Light-fuelled dissipative replication and selection in adaptive biomimetic chemical networks

Éva Bartus[1,2], Beáta Mag[1], Áron Bajcsi[1], Attila Tököli[1], Gábor Kecskeméti[1], Edit Wéber[1], Zoltán Kele[1], Tamás A. Martinek[1,2]*

Affiliations:

[1] Department of Medical Chemistry, University of Szeged, Dóm tér 8, H-6720 Szeged, Hungary [2] MTA-SZTE Biomimetic Systems Research Group, University of Szeged, Dóm tér 8, H-6720 Szeged, Hungary

*Corresponding author. Email: martinek.tamas@med.u-szeged.hu

Evolvability of the chemical replicator systems requires non-equilibrium energy dissipation, effective death pathways and transfer of structural information in the autocatalytic cycles. We engineered a chemical network with peptidic foldamer components, where UV light fuelled dissipative sequence-dependent exponential replication and replicator decomposition. The light-harvesting formation-recombination cycle of the thiyl radicals was coupled with the molecular recognition steps in the replication cycles. Thiyl radical-mediated chain reaction was responsible for the replicator death. The competing and kinetically asymmetric replication and decomposition processes led to light intensity-dependent selection and competitive exclusion. Dynamic adaptation to the energy input and the selection factor maximised the dissipation rate in the regime of exponential growth. The results contribute to the development of chemically evolvable replicator systems.

Introduction

Chemical networks mimicking evolution need to operate dynamically far from equilibrium[1], which is essential for their open-ended adaptive behaviour. The dynamic kinetic stability in such systems results from the balance between the asymmetric formation and destruction processes driven by the dissipation of energy harvested from the environment[2-4]. Besides metabolism and compartmentalisation, dissipative replication and selection leading to competitive exclusion are crucial components for modelling Darwinian evolution. Non-equilibrium dynamics occurs in dissipative chemical networks[2,5,6], which rely on an energy-harvesting catalytic cycle covering the entropy production of the system. Engineered dissipative systems[3,7] attain off-equilibrium states present in the non-covalent assembly of the building blocks[8-10]. The dissipative self-organisation of material can be a source of structural complexity[11-13] linked with the emergence of life.

Energy input can influence chemical replication systems in two ways. First, chemical[13] or light energy[14,15] can produce the low-energy precursors, which leaves the rate constant of the replication intact. Second, the energy absorption directly modifies the rate constants by producing high-energy transition states creating kinetic asymmetry in the dissipative replication. Our goal was to couple the external energy source with the transition state of replication, thus driving the system to exponential growth. Successful kinetic coupling of molecular recognition with a dynamic covalent rearrangement is possible if the reaction rates are comparable[4,16]. The association rate of binding is under diffusion control, while affinity determines dissociation. Thus, diffusion-controlled covalent chemistry was required, of which conversion rate can be manipulated by the intensity of the energy input. We hypothesised that the diffusion-controlled recombination of UV light-fuelled thiyl radicals[17] could be

1

successfully coupled with the replication without light-induced damage of the biotic components. We also aimed an energy-dependent decomposition for efficient selection, but kinetic asymmetry required a separate mechanism from replication. Radical substitution is possible between thiyl and disulphides in chain reactions, which can facilitate replicator breakdown. Theoretical models revealed that in the presence of multiple energy-driven asymmetric reaction pathways, chemical networks tend to select the most dissipative states that strongly match with the available source of energy[2,4,18]. This principle suggested a dissipative replication and selection mechanism, which can adapt in an external energy-dependent manner.

Designed helical peptides can transfer structural information in autocatalytic processes[19,20], and exponential replication has been achieved for peptidic helices[21]. Helical foldamers are excellent models to construct such a complex system because the folding step is programmable independently of the biomimetic recognition surface[22,23]. Moreover, short peptidomimetic foldamers tend to self-associate in solution[24], which is an advantageous feature in terms of auto- and cross-catalytic templating. We set out to test the concept of dissipative replication and selection in a multicomponent system, wherein the energy-harvesting thiyl chemistry links the biomimetic foldamer sequences.

Here, we show that a UV light-fuelled dissipative chemical network with several individual components can carry out dissipative replication and selection in a light intensity-dependent manner.

Results

### Design of the dissipative chemical network

We constructed the reaction network using hexameric β-peptide foldamers designed to fold into compact helical structures (Fig. 1). The sequences contained two variable positions (**Xaa^1** and **Xaa^2**), where proteinogenic side chains were incorporated. These can successfully probe protein surfaces[22], and the ordered secondary structure promotes self-association[24]. Cys residues were attached to the C-terminal, which allowed the disulphide linkage between the foldamer segments (dimers, **X^{1}X^2-X^1'X^2'**) and glutathione (monomers, **X^{1}X^2-SG**). There was no free thiol group present in the system, and pH 7.0 was set to eliminate the disulphide exchange through the thiolate-mediated nucleophile mechanism. Disulphide rearrangement reactions were driven by UV irradiation (365 nm) at constant temperature (303 K). Homolytic cleavage yielded the high-energy thiyl radical intermediates, which facilitated two mechanisms (Fig. 1): radical chain reaction and direct radical recombination (see Supporting information for the detailed kinetic description). The chain reaction is initiated by light absorption, multiple reaction steps occur *via* radical transfer, and it is terminated by the diffusion-controlled collision of the freely diffusing thiyl radicals. Energy dissipation occurs in the termination step of the chain reaction. Direct radical recombination is catalysed by the molecular recognition between the components, and it requires the absorption of two photons during the lifetime of the complexes to produce a dimer. The direct radical recombination pathway dissipates energy in each reaction step leading to the formation of a dimer.

In this study, we chose 12 different side-chain combinations based on their tendency to self-associate and the ability to bind to a template protein (calmodulin)[25]. This setup allowed 78 different dimers and 12 glutathione protected monomers (Fig. 1, Supplementary Table 1), and UV irradiation added 13 radical intermediates to the system. Binding between the components and the shared building blocks further increased the number of the actual nodes in the reaction network. The system was tested with and without protein templating. The trajectories of the

dynamic adaptation were monitored by using HPLC-MS analysis of the stable dimers and monomers.

Figure 1. Dissipative chemical network designed for dissipative replication and selection. (**a**) General scheme for coupling the formation-recombination cycle of the UV light-induced thiyl radicals to the template-directed replication (left) and the non-autocatalytic spontaneous and protein-templated processes (right). Assumed radical chain reaction pathways for decomposition and spontaneous synthesis are indicated in the centre (**b**) Schematic representation and the corresponding general sequences of the foldamer library: X^1X^2-**SG**: glutathione protected monomers, X^1X^2-$X^{1'}X^{2'}$: disulphide-linked dimers. SG indicates the glutathione (γ-L-glutamyl-L-cysteinyl-glycine) and ACHC stands for 1S,2S-2-aminocyclohexanecarboxylic acid, which promotes helical folding. In the highlighted positions X^1 and X^2, β^3-amino acids with proteinogenic side chains were incorporated in the following combinations: IF, KW, LW, QW, RW, RF, SW, TW, VW, WF, WW and YF. One-letter codes correspond to the side chains in the standard α-amino notation.

Dissipative template-directed replication and selection in the foldameric reaction network

We tested the behaviour of the foldameric reaction network upon exposure to UV irradiation. The power density was increased linearly in four steps up to the maximum value available in our setup (5.10 mW cm^{-2}), and the concentration of each component was monitored. At 25% light intensity, we could not detect dimer formation. At 50% and above, dimers were observed, and the system attained steady state in 5 hours (Fig. 2a, Supplementary Fig. 1) without degradation of the peptidic sequences. The increasing light intensity caused a non-linear sequence-dependent growth of the dimer population (Fig. 2b). For the most amplified dimer, elevating the power density from 50% to 100% led to a 130.2 times concentration increase

(Fig. 2c). The amplification factors were above 72.5 for the best ten sequences. The lowest-ranked dimers did not display significant light intensity-dependent behaviour. Enrichment of the aromatic and aliphatic hydrophobic side chains was detected for the set of the ten most populated sequences relative to the complete set of dimers (Fig. 2d). In parallel, depletion of the cationic and polar residues was measured at the peripheral positions (1 and 1'), indicating the role of the hydrophobically-driven association processes.

The system dynamically adapted to the energy input, which is a characteristic of a dissipative system. The sequence-dependent non-linear response indicated the presence of a template-directed auto-, cross-catalytic or both type of replication. To gain quantitative support for the dissipative replication process, we analysed the experimental data in the dynamic model framework for chemical evolution[26,27], which we extended to our dissipative system. A rate equation was constructed, including the direct radical recombination and chain reaction mechanisms for spontaneous synthesis, replication and breakdown of the dimers based on the dissipative reaction network given in Figure 1 (see Supplementary Text for details). The time evolution of the system was simulated by numeric integration of the dynamic model with variable rate constants. Non-linear regressions were carried out against all data points measured for the individual dimer components at three light intensities (Fig. 2a and c, Supplementary Fig. 1, Supplementary Table 2). The experimental data validated the dynamic model, which confirmed that direct radical recombination was responsible for the dimer synthesis, while breakdown occurred through the chain reaction mechanism. Moreover, the dominant pathway for dimer production was the autocatalytic replication after a short initial period of non-autocatalytic seeding (Fig. 2e). Exponential growth was observed, which was kept in this regime by the breakdown process and not by the depletion of the monomers. Combinations of building blocks **YF**, **WF** and **IF** appeared dominantly among the best replicators. Their spontaneous synthesis rate constants were uniformly low, and the breakdown rate constants correlated with the replication rate constants (Supplementary Fig. 3). This pattern strongly suggested that the templating stabilised only the transition states of formation, and the replicators were available both for exponential autocatalysis and effective decomposition. The sequence similarity and the matching replication behaviour supported that the replication cycles of these sequences are coupled through cross-catalysis, and they formed a quasispecies[28]. Notably, the steady state analysis of the model (see Supplementary Text for details) explained the hyperbolic light intensity-dependence of the dimer concentration (Fig. 2b). This relationship is the direct consequence of the dissipative template-directed autocatalytic replication and the competing chain reaction-mediated decomposition. Together with the sequence-dependent amplification, these quantitative results proved that the system undergoes dissipative replication and selection.
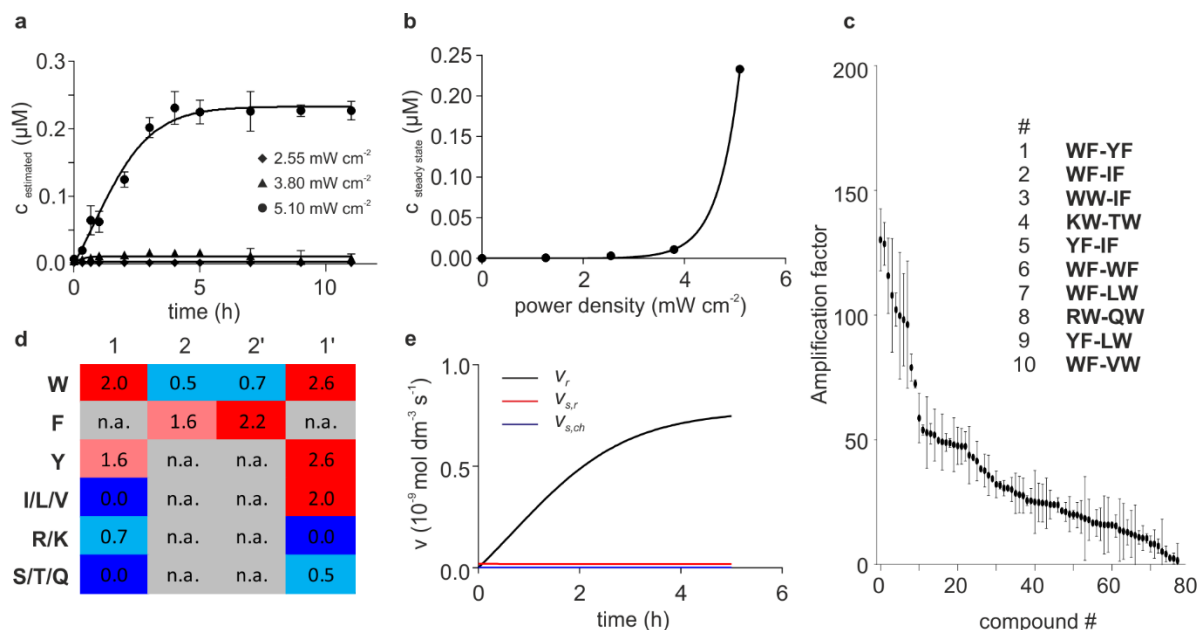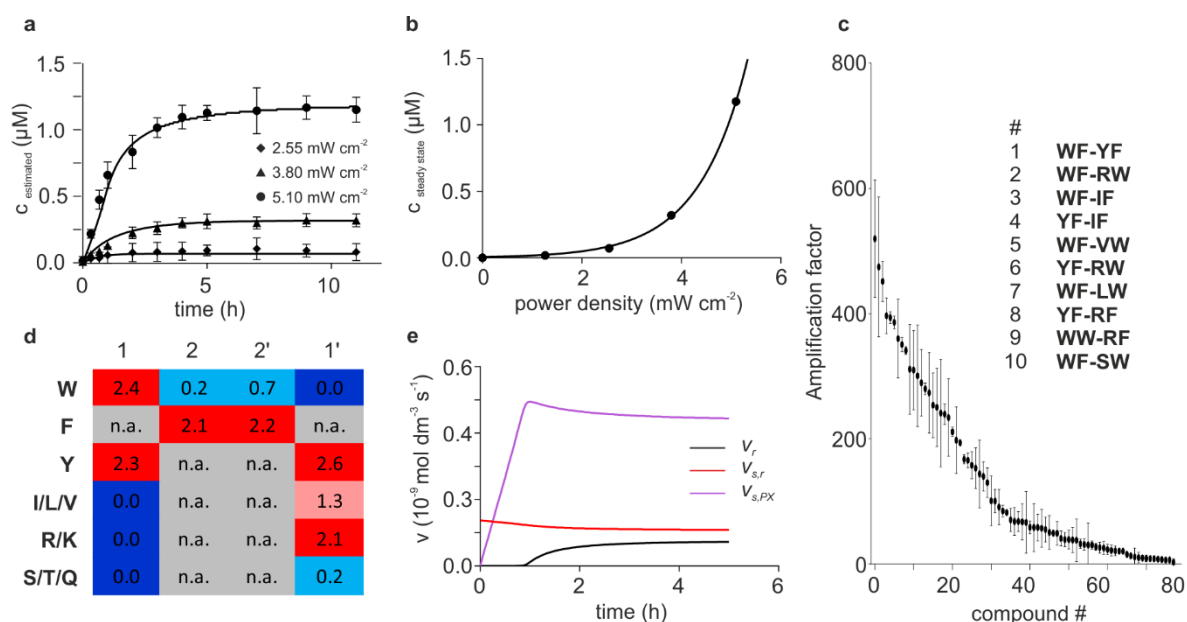
Figure 2. Light intensity-dependent dissipative replication of the foldamer system. (**a**) Time-dependent concentration of a representative dimer (**WF-YF**) irradiated at different light intensities: 2.55 mW cm^{-2} (diamonds), 3.80 mW cm^{-2} (triangles), 5.10 mW cm^{-2} (circles). Solid curves display the fitted kinetic simulations based on the dissipative replication and decomposition model. (**b**) Light intensity-dependent steady state concentrations for **WF-YF** (circles). The fitted curve indicates the simulated hyperbolic relationship between the steady state concentrations and the illumination power density. (**c**) Amplification factors obtained upon increasing light intensity from 50% to 100% and the ten most amplified sequences (inset). (**d**) Enrichment of the proteinogenic side chains in the peripheral (1, 1') and the central (2, 2') positions of the ten most amplified dimers (n.a. stands for 'not applicable'). (**e**) Rates of replication (v_r: black), non-autocatalytic synthesis *via* direct radical recombination ($v_{s,r}$: red) and radical chain reaction ($v_{s,ch}$: blue) obtained from the fitted dynamic model for **WF-YF**.

Adaptation of the system to protein templating as selection factor

In the next step, we tested the ability of the system to adapt dynamically to a potential selection factor, that is, to the presence of a protein interacting with specific components of the system. Before the experiment, UV-induced deterioration of the protein was ruled out for the period of the measurements (see Supplementary Methods and Supplementary Fig. 2). The growth of the steady state dimer population upon increasing the light intensity remained hyperbolic (Fig. 3a), and the concentration of the dimers displayed a marked increase (Fig. 3b) relative to the pure foldamer system. The distribution of the amplification factors revealed significant differences (Fig. 3c). Elevating light intensity from 50% to 100% caused amplifications of the best ten dimers in the range 520.0 – 289.5, whereas the lowest amplified sequences displayed values around 6.0. The side chain selection also changed relative to the pure foldamer system (Fig. 3d). Enrichment of Trp and the cationic side chains (Arg/Lys) was observed only at one of the peripheral positions, and Tyr dominated in all positions. This pattern was in line with the recognition motif of the target[29], indicating that protein binding had a strong influence on the outcome of the dissipative selection.

The quantitative analysis of the experimental data (Fig. 3a) confirmed that the protein increased the non-autocatalytic dimer synthesis rate constants by opening a new templated route (Supplementary Table 3, Supplementary Fig. 3) for the dimers that bind the protein with both

helix segments simultaneously (e.g., **WF-RW**). However, the data strongly suggested a biexponential behaviour, and accordingly, the dynamic model constructed for the pure foldamer sample did not provide a satisfactory description of the system. Unexpectedly, the macromolecule opened a protein-dependent autocatalytic pathway (see Supplementary Text and Supplementary Fig. 4). Independent ITC data revealed the possibility of sequential binding of two dimers to the protein (Supplementary Fig. 5). This binding mode facilitated the formation of a protein-dimer hybrid template responsible for the protein-dependent autocatalytic replicator synthesis. The description of the protein-templated system in a single theoretical framework was only possible by adding the corresponding rate term to the dynamic model (see Supplementary Text). This rate component is also of first order in replicator concentration, but the limited protein concentration breaks down the exponential growth. The self-replication and the protein-dependent autocatalytic pathways contributed to the dimer synthesis at comparable levels (Fig. 3e). These replicators displayed hydrophobic side chains and lacked cationic functions required by the native binding motif of the protein (Supplementary Fig. 3).

Figure 3. Light intensity-dependent dissipative replication and selection in the protein-templated foldamer system. (**a**) Time-dependent concentration of a representative dimer (**WF-RW**) irradiated at different light intensities: 2.55 mW cm^{-2} (diamonds), 3.80 mW cm^{-2} (triangles), 5.10 mW cm^{-2} (circles). Solid curves display the fitted kinetic simulations based on the dissipative replication and decomposition model. (**b**) Light intensity-dependent steady state concentrations for **WF-RW** (circles). The fitted curve indicates the simulated hyperbolic relationship between the steady state concentrations and the illumination power density. (**c**) Amplification factors obtained upon increasing light intensity from 50% to 100% and the ten most amplified sequences (inset). (**d**) Enrichment of the proteinogenic side chains in the peripheral (1, 1') and the central (2, 2') positions of the ten most amplified dimers (n.a. stands for 'not applicable'). (**e**) Rates of replication (v_r: black), the protein-dependent autocatalytic pathway ($v_{s,PX}$: purple) and the non-autocatalytic synthesis *via* direct radical recombination ($v_{s,r}$: red) obtained from the fitted dynamic model for **WF-RW**.

Dissipative adaptation leads to energy-dependent competitive exclusion

The exponential growth and the effective decomposition mechanism endow the replicators with a potential ability for competitive exclusion in the presence of a selection factor, such as the limited concentration of the protein binding sites[30]. To study this effect, we calculated the protein-dependent amplification factors (protein-templated system relative to the pure foldamer network) at the respective irradiation intensities (Fig. 4a). The most selected replicators showed a marked enhancement of the protein-induced amplification with the increasing power density. For the dimers in the intermediate affinity range, amplifications were suppressed at the highest light intensity. The low-affinity dimers gave little energy-dependent response to the protein template. Altogether, this complex energy-dependent behaviour supported the presence of the competitive exclusion in the dissipative system. To capture the quantitative differences in the amplification distributions, Shannon diversity indices (I_{Sh}) were calculated (Fig. 4b, see Supplementary Text for calculation). Decreasing diversity index was found with the increasing power density, which was a proxy for improving competitive exclusion. This result was in accord with the competition for the limited amount of protein binding sites. As the energy input efficiently increased the concentration of the high-affinity sequences, a displacement of the low-affinity replicators occurred. To confirm this hypothesis, we carried out measurements at different protein concentrations with at 100% light intensity (Fig. 4c). As expected, we observed a lowered competitive exclusion effect at the elevated protein concentration (Fig. 4d). Decreasing the template concentration was also detrimental for the exclusion effect because the self-templated processes successfully outcompeted the protein-dependent selection factor.
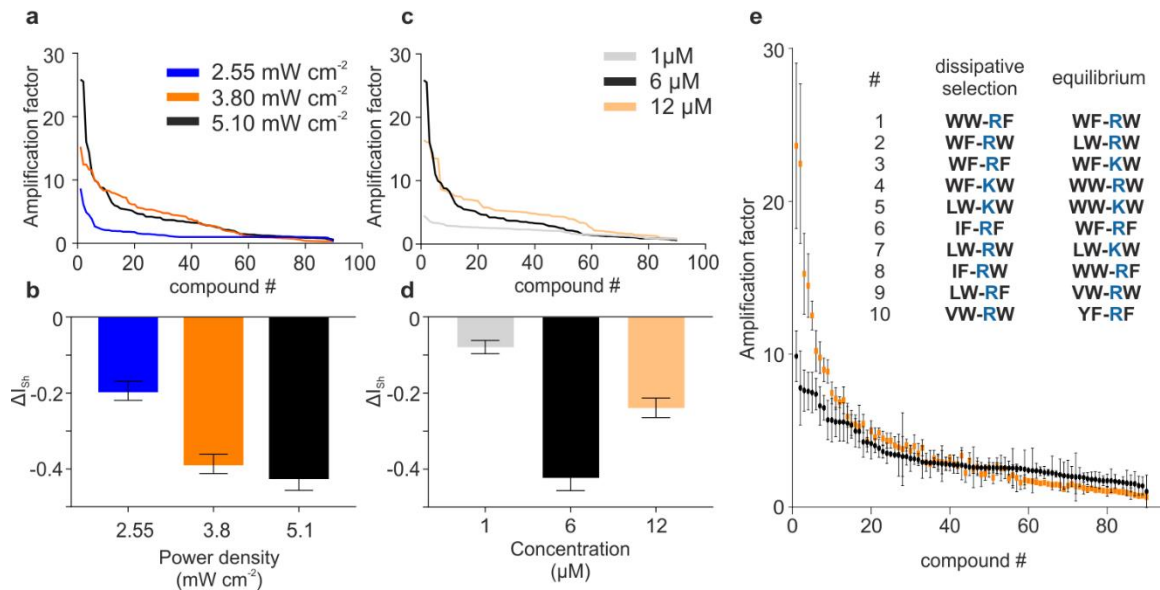

Figure 4. Protein-dependent amplification factors and competitive exclusion in the dissipative system. Protein-dependent amplification profiles (**a**) and Shannon diversity decrease (ΔI_{Sh}) (**b**) obtained for the dissipative systems at light intensities of 2.55 mW cm^{-2} (blue), 3.80 mW cm^{-2} (orange), 5.10 mW cm^{-2} (black). Protein-dependent amplification profiles (**c**) and Shannon diversity decrease (ΔI_{Sh}) (**d**) for the dissipative systems at 100 % power density and protein concentrations of 1 μM (light grey), 6 μM (black) and 12 μM (light orange). (**e**) Amplification profiles of the dissipative (orange) and the equilibrium (black) systems. The table in the inset lists the ten most amplified components in the dissipative steady-state and equilibrium[25]. Shannon diversity decrease values (ΔI_{Sh}) were calculated relative to a theoretical maximum diversity case, where all amplification was uniform (I_{Sh}^{max}). Detailed amplification values are given in Supplementary Tables 4-6.

These findings supported that the energy input steered the system away from the equilibrium state. In the next step, we directly compared the UV-fuelled dissipative system with the thermodynamically controlled one generated by the thiolate-mediated nucleophilic mechanism. We performed separate experiments in glutathione redox buffer at pH 8.0[25]. The amplification factors for the best ligands were significantly higher for the dissipative system than those for the equilibrium setup (Fig. 4e), indicating the distance between the two systems. Thus, the external energy-driven competitive exclusion led to superior selection efficiency. Despite the fundamental difference between the kinetic and thermodynamic control, the sets of selected ligands overlapped considerably (Fig. 4e inset). This result connotes that the dissipative selection occurred in correlation with the affinity of the molecular recognition steps. Two of the best ligands (**WW-RF** and **WF-RW**) were independently characterised concerning their affinities to the template, and low nanomolar interactions were detected at the orthosteric interface of the protein (Supplementary Fig. 5).

The dissipation rate is maximised during adaptation in the regime of exponential growth.

According to the theoretical predictions[4], it was our initial hypothesis that the system adapts to the energy input and the selection factor by maximising the rate of dissipation. There are two dissipative mechanisms in our system. First, dissipation occurs through the mechanism of direct radical recombination. In this case, the corresponding dissipation rate component is proportional with the sum of the reaction rates associated with the formation of the dimers. Second, the replicator breakdown process is coupled to the dissipative chain reaction mechanism. We initially assumed in the dynamic model that the freely diffusing radical concentration was constant at a specific light intensity (Supplementary Text). Therefore, the overall dissipation rate of the chain reaction did not change during the composition-dependent adaptation. On this ground, we concluded that the change in the total rate of dissipation was caused by the net change in the rate of dimer formation.
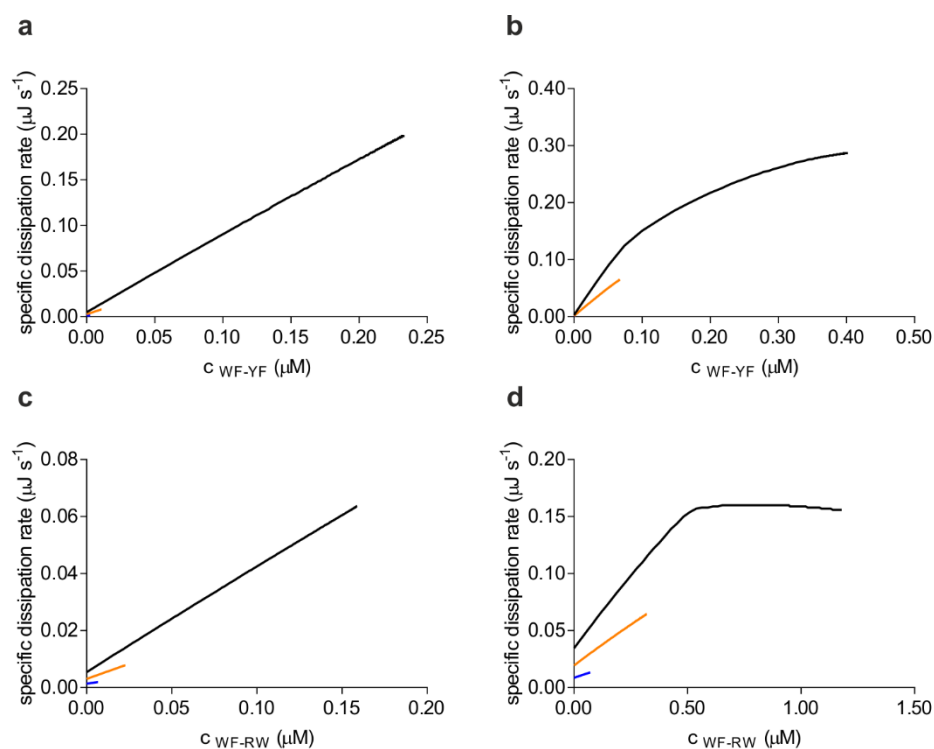
Figure 5. Dissipation rate changes during the composition-dependent adaptation. Dependence of the specific dissipation rate on the concentration of **WF-YF** in the pure foldameric replicating system (**a**) and the protein-templated sample (**b**). Dependence of the specific dissipation rate on the concentration of **WF-RW** in the pure foldameric replicating system (**c**) and the protein-templated sample (**d**). Dissipation rates are displayed at light intensities of 2.55 mW cm^{-2} (blue), 3.80 mW cm^{-2} (orange), 5.10 mW cm^{-2} (black).

The specific dissipation rates were estimated for the individual replicators with the disulphide binding energy of 251 kJ/mol. The adaptation was visualised by plotting the dissipation rates against the concentration of the replicators (Fig. 5). For replicators, where the self-templated replication rate was sufficiently large (Fig. 2e, Fig 5a, b and c), the dissipation rate was a monotonously increasing function of the dimer concentration. The slope of the dissipation rate increase was affected by the biexponential behaviour in the presence of the protein. Until reaching the steady state, both the concentration of the replicators and the corresponding dissipation rate increased. Thus, the system reached the maximum level of the dissipation rate available under the conditions applied. For replicators with dominant protein-templated synthesis mechanisms, the dissipation rate increased only in the regime of exponential growth (Fig. 5d). The monomer depletion-driven decay overcompensated the exponential replication, which led to a negative slope for the dissipation rate as the system approached the dynamic kinetic stability.

Discussion

We successfully coupled the diffusion-controlled light-harvesting thiyl radical chemistry with the molecular recognition processes occurring in a complex foldameric network. Disulphide linkage has a long history, and its nucleophilic exchange mechanism is currently popular in systems chemistry applications[31,32]. The performance of the UV light-induced homolytic cleavage and recombination cycle of the disulphide bond to drive dissipative processes extended its applicability beyond the thiolate-mediated dynamics. The minimal proteomimetic sequences with micromolar interactions could replicate because the high-energy radical intermediates facilitated a rapid relaxation of the transition state complex toward the dimer formation. This finding indicates that the weak binding between primitive structures facilitates replication if the dynamic covalent rearrangement is fast enough. These properties render this system a valuable tool to study dissipative replication and selection starting at a low level of replicator complexity.

The radical chain reaction of the thiyl moiety facilitated an external energy-driven independent replicator death mechanism without physical separation of the pathways[33,34]. Together with the exponential growth of the replicator concentration, this feature is essential for evolvability because these make strongly differential distribution or competitive exclusion possible. With a protein template in the system as a selection factor, the foldameric replicator population competed for the limited binding site concentration leading to energy-dependent exclusion. We observed improved efficiencies for the light-fuelled dissipative selection compared with the equilibrium system run with the same composition. Notably, for the dissipative method, the amplification factors were dependent on the light intensity. Thus, light not only switched processes on and off, but the energy influx also drove the system to off-equilibrium steady states ratcheting up the fittest sequences[2,35]. It is a general property of the equilibrium DCL systems that selection efficiency increases with the decreasing template concentration[36], and the limiting factor is the sensitivity of the analytical method. Dissipative selection fundamentally differs because selection efficiency can be maximised with the template

concentration. For practical applications, such as fragment-based development of ligands for protein recognition[37], the critical indicator is the rate constant of the non-autocatalytic synthesis. The best binders tend to land all segments simultaneously on the target; therefore, the autocatalytic processes play a minor role, and the protein-templated synthesis dominates.

Mimicking the features of life in chemical systems, such as dissipative adaptation[4,38], helps understand the chemical mechanisms of spontaneous emergence of complexity and create functional chemical systems artificially. Pioneering experiments with dissipative self-assembling systems established the principles that govern chemical energy[39-41] or light-driven[42,43] trajectories to off-equilibrium states generating spatial proximity-based order. In this work, the species-level analysis of the system facilitated a quantitative kinetic analysis of the non-equilibrium chemical network. The results confirmed the presence of the dissipative replication and the effective death mechanism. Moreover, rate components revealed that the system maximises dissipation rate during adaptation in the exponential regime of growth. These findings are in accord with the principle of adaptation through maximising the dissipation rate. In our system, this is equivalent to the maximisation of the rate of the autocatalytic processes.

Although the system presented here displayed features essential for chemical evolution, the prebiotic chemistry is beyond the scope of this study. However, the chemical availability of primitive Cys-containing peptides is supported by the prebiotic Cys-catalysed amino acid and peptide synthesis[44,45]. These findings suggest that the thiyl radical-mediated dissipative replication of short folding peptidic sequences is an intriguing mechanism[46] potentially contributing to the transition from prebiotic chemical networks to biotic evolution.

Methods

UV-fuelled disulphide exchange reaction. Twelve different foldamer-SG disulphides were dissolved in 20 mM HEPES, 150 mM NaCl, 2 mM $CaCl_2$, 3 mM NaN_3 (pH = 7.0) each one at 10 μM concentration without the protein (control) and with the protein at appropriate concentration. The reaction mixtures were transferred separately into quartz cuvettes having PTFE stopper and kept under argon atmosphere during the experiment. Solutions were stirred at 150 RPM and kept at the constant temperature of 303 ± 1 K *via* air cooling system (modified Jasco Jetstream 2 Plus Column Thermostat). Temperature was monitored with a laser gun thermometer. Continuous illumination of the samples was carried out with UVL-28 EL Series UV Lamp (Analytic Jena US, Upland, CA). The power density and its position/distance dependence and the emission spectra of the lamp were determined before the experiments (Supplementary Fig. 8), and the irradiation intensity was controlled by the distance between the lamp and the sample. 200 μL samples were taken from the reaction mixture at each time point and quenched with 100 μL of 10% TFA in water to significantly slow down any other disulphide exchange reaction in the mixture until the analysis. The product distribution of the samples was analysed by HPLC/ESI-MS measurements.

LC-MS measurements and MS data analysis. LC-MS analysis was performed with a Dionex UltiMate 3000 HPLC system interfaced to an LTQ ion trap mass spectrometer (Thermo Electron Corp., San Jose, CA, USA). Samples were injected onto an Aeris[TM] Widepore XB-C18 (250 x 4.6 mm, particle size: 3.6 μm, pore size 100Å) analytical HPLC column using gradient elution 5-80% solution B during 25 minutes at 0.7 mL min^{-1} flow rate. Eluent composition was 0.1% formic acid in distilled water (Solution A) and 0.1% formic acid in

acetonitrile (Solution B). The MS instrument was operated in the positive-ion mode using the equipped HESI-II source with the following parameters: capillary temperature: 350°C; spray voltage: 3.0 kV; source heater temperature: 250°C; sheath gas flow: 30 mL min^{-1}; aux gas flow: 10 mL min^{-1}. Mass spectra were acquired in full scan mode from 200 to 2000 m/z range. Thermo Xcalibur 2.2 software was used for peak identification and integration. The 96% of the foldameric building blocks could be resolved independently via HPLC-MS/MS measurements based on molecular weight, MS fragmentation pattern and retention time considering the relative hydrophobicity of the side-chains. Those components which could not be resolved independently were integrated together and averaged. A representative raw file for the library was utilised to create a processing method where each sample component was associated with a chromatographic peak based on the previously identified mass (m/z) and retention time (Supplementary Table 1). Using the ICIS peak detection algorithm, the general detection and integration criteria were smoothing points: 5, baseline window: 60, area noise factor: 5, peak noise factor: 10. All raw data files were reprocessed with these processing setups together and analysed. Errors in peak identification during the automatic processing were corrected manually.

References

1   Adamski, P. *et al.* From self-replication to replicator systems en route to de novo life. *Nature Reviews Chemistry* **4**, 386-403, doi:10.1038/s41570-020-0196-x (2020).

2   Ragazzon, G. & Prins, L. J. Energy consumption in chemical fuel-driven self-assembly. *Nature nanotechnology* **13**, 882-889, doi:10.1038/s41565-018-0250-8 (2018).

3   Singh, N., Formon, G. J., De Piccoli, S. & Hermans, T. M. Devising Synthetic Reaction Cycles for Dissipative Nonequilibrium Self-Assembly. *Advanced Materials* **32**, 1906834 (2020).

4   England, J. L. Dissipative adaptation in driven self-assembly. *Nature nanotechnology* **10**, 919-923, doi:10.1038/nnano.2015.250 (2015).

5   Mattia, E. & Otto, S. Supramolecular systems chemistry. *Nature nanotechnology* **10**, 111-119, doi:10.1038/nnano.2014.337 (2015).

6   van Rossum, S. A. P., Tena-Solsona, M., van Esch, J. H., Eelkema, R. & Boekhoven, J. Dissipative out-of-equilibrium assembly of man-made supramolecular materials. *Chemical Society Reviews* **46**, 5519-5535, doi:10.1039/c7cs00246g (2017).

7   Rieß, B., Grötsch, R. K. & Boekhoven, J. The design of dissipative molecular assemblies driven by chemical reaction cycles. *Chem* **6**, 552-578 (2020).

8   Sorrenti, A., Leira-Iglesias, J., Sato, A. & Hermans, T. M. Non-equilibrium steady states in supramolecular polymerization. *Nature communications* **8**, 15899, doi:10.1038/ncomms15899 (2017).

9   Kathan, M. & Hecht, S. Photoswitchable molecules as key ingredients to drive systems away from the global thermodynamic minimum. *Chemical Society Reviews* **46**, 5536-5550, doi:10.1039/c7cs00112f (2017).

10   Nanda, J. *et al.* Emergence of native peptide sequences in prebiotic replication networks. *Nature communications* **8**, 434, doi:10.1038/s41467-017-00463-1 (2017).

11   Green, L. N. *et al.* Autonomous dynamic control of DNA nanostructure self-assembly. *Nature Chemistry* **11**, 510-520 (2019).

12   Liu, Z. *et al.* Harnessing chemical energy for the activation and joining of prebiotic building blocks. *Nature Chemistry* **12**, 1-6 (2020).

13   Morrow, S. M., Colomer, I. & Fletcher, S. P. A chemically fuelled self-replicator. *Nature communications* **10**, 1011, doi:10.1038/s41467-019-08885-9 (2019).

14   Monreal Santiago, G., Liu, K., Browne, W. R. & Otto, S. Emergence of light-driven protometabolism on recruitment of a photocatalytic cofactor by a self-replicator. *Nature Chemistry* **12**, 603-607, doi:10.1038/s41557-020-0494-4 (2020).

15   Dadon, Z., Samiappan, M., Wagner, N. & Ashkenasy, G. Chemical and light triggering of peptide networks under partial thermodynamic control. *Chemical communications (Cambridge, England)* **48**, 1419-1421, doi:10.1039/c1cc14301h (2012).

16   Maiti, S., Fortunati, I., Ferrante, C., Scrimin, P. & Prins, L. J. Dissipative self-assembly of vesicular nanoreactors. *Nature Chemistry* **8**, 725-731, doi:10.1038/nchem.2511 (2016).

17   Du, X. *et al.* Reversible and Rewritable Surface Functionalization and Patterning via Photodynamic Disulfide Exchange. **27**, 4997-5001, doi:https://doi.org/10.1002/adma.201501177 (2015).

18   Penocchio, E., Rao, R. & Esposito, M. Thermodynamic efficiency in dissipative chemistry. *Nature communications* **10**, 1-5 (2019).

19   Lee, D. H., Granja, J. R., Martinez, J. A., Severin, K. & Ghadiri, M. R. A self-replicating peptide. *Nature* **382**, 525-528, doi:10.1038/382525a0 (1996).

20   Amit, M., Yuran, S., Gazit, E., Reches, M. & Ashkenasy, N. Tailor-Made Functional Peptide Self-Assembling Nanostructures. **30**, 1707083, doi:https://doi.org/10.1002/adma.201707083 (2018).

21   Issac, R. & Chmielewski, J. Approaching exponential growth with a self-replicating peptide. *J Am Chem Soc* **124**, 6808-6809, doi:10.1021/ja026024i (2002).

22   Tököli, A. *et al.* Proteomimetic surface fragments distinguish targets by function. *Chemical Science* **11**, 10390-10398, doi:10.1039/D0SC03525D (2020).

23   Fisher, B. F., Hong, S. H. & Gellman, S. H. Helix Propensities of Amino Acid Residues via Thioester Exchange. *Journal of the American Chemical Society* **139**, 13292-13295, doi:10.1021/jacs.7b07930 (2017).

24   Martinek, T. A. *et al.* Effects of the alternating backbone configuration on the secondary structure and self-assembly of beta-peptides. *J Am Chem Soc* **128**, 13539-13544, doi:10.1021/ja063890c (2006).

25   Bartus, É. *et al.* De Novo Modular Development of a Foldameric Protein–Protein Interaction Inhibitor for Separate Hot Spots: A Dynamic Covalent Assembly Approach. *ChemistryOpen* **6**, 236-241 (2017).

26   Higgs, P. G. Chemical Evolution and the Evolutionary Definition of Life. *Journal of Molecular Evolution* **84**, 225-235, doi:10.1007/s00239-017-9799-3 (2017).

27   von Kiedrowski, G. in *Bioorganic Chemistry Frontiers*   (eds Hermann Dugas & Franz P. Schmidtchen) 113-146 (Springer Berlin Heidelberg, 1993).

28   Eigen, M., McCaskill, J. & Schuster, P. Molecular quasi-species. *The Journal of Physical Chemistry* **92**, 6881-6891, doi:10.1021/j100335a010 (1988).

29   Mruk, K., Farley, B. M., Ritacco, A. W. & Kobertz, W. R. Calmodulation meta-analysis: predicting calmodulin binding via canonical motif clustering. *The Journal of general physiology* **144**, 105-114, doi:10.1085/jgp.201311140 (2014).

30   Szathmáry, E. & Gladkih, I. Sub-exponential growth and coexistence of non-enzymatically replicating templates. *Journal of theoretical biology* **138**, 55-58, doi:10.1016/s0022-5193(89)80177-8 (1989).

31   Diemer, V. *et al.* A cysteine selenosulfide redox switch for protein chemical synthesis. *Nature communications* **11**, 2558, doi:10.1038/s41467-020-16359-6 (2020).

32   Canal-Martín, A. & Pérez-Fernández, R. Biomimetic selenocystine based dynamic combinatorial chemistry for thiol-disulfide exchange. *Nature communications* **12**, 163, doi:10.1038/s41467-020-20415-6 (2021).

33   Corbett, A. D., Cheeseman, J. D., Kazlauskas, R. J. & Gleason, J. L. Pseudodynamic Combinatorial Libraries: A Receptor-Assisted Approach for Drug Discovery. *Angewandte Chemie (International ed. in English)* **43**, 2432-2436 (2004).

34   Ji, Q., Lirag, R. C. & Miljanic, O. S. Kinetically controlled phenomena in dynamic combinatorial libraries. *Chemical Society Reviews* **43**, 1873-1884, doi:10.1039/c3cs60356c (2014).

35   Astumian, R. D. Kinetic asymmetry allows macromolecular catalysts to drive an information ratchet. *Nature communications* **10**, 1-14 (2019).

36   Ludlow, R. F. & Otto, S. The impact of the size of dynamic combinatorial libraries on the detectability of molecular recognition induced amplification. *J Am Chem Soc* **132**, 5984-5986, doi:10.1021/ja1013689 (2010).

37   Murray, C. W. & Rees, D. C. The rise of fragment-based drug discovery. *Nature Chemistry* **1**, 187-192, doi:10.1038/nchem.217 (2009).

38   Ashkenasy, G., Hermans, T. M., Otto, S. & Taylor, A. F. Systems chemistry. *Chemical Society Reviews* **46**, 2543-2554, doi:10.1039/c7cs00117g (2017).

39   Liu, L. *et al.* Enzyme-free synthesis of natural phospholipids in water. *Nature Chemistry* **12**, 1029-1034 (2020).

40   Pezzato, C. & Prins, L. J. Transient signal generation in a self-assembled nanosystem fueled by ATP. *Nature communications* **6**, 7790, doi:10.1038/ncomms8790 (2015).

41   Boekhoven, J., Hendriksen, W. E., Koper, G. J., Eelkema, R. & van Esch, J. H. Transient assembly of active materials fueled by a chemical reaction. *Science* **349**, 1075-1079 (2015).

42   Remon, P. *et al.* Light-driven control of the composition of a supramolecular network. *Chemical Communications* **55**, 4335-4338, doi:10.1039/c9cc00922a (2019).

43   Kundu, P. K. *et al.* Light-controlled self-assembly of non-photoresponsive nanoparticles. *Nature Chemistry* **7**, 646-652 (2015).

44   Canavelli, P., Islam, S. & Powner, M. W. Peptide ligation by chemoselective aminonitrile coupling in water. *Nature* **571**, 546-549 (2019).

45   Foden, C. S. *et al.* Prebiotic synthesis of cysteine peptides that catalyze peptide ligation in neutral water. *Science* **370**, 865-869 (2020).

46   Guseva, E., Zuckermann, R. N. & Dill, K. A. Foldamer hypothesis for the growth and sequence differentiation of prebiotic polymers. *Proceedings of the National Academy of Sciences* **114**, E7460, doi:10.1073/pnas.1620179114 (2017).

Data availability

All data is available in the main text or the supplementary materials. All data and materials used in the analysis is available to any researcher for purposes of reproducing or extending the analysis.

Acknowledgements

Funding

Author contributions

Competing interests

Authors declare no competing interests.

Supplementary Information for

Light-fuelled dissipative replication and selection in adaptive biomimetic chemical networks

Éva Bartus[1,2], Beáta Mag[1], Áron Bajcsi[1], Attila Tököli[1], Gábor Kecskeméti[1], Edit Wéber[1], Zoltán Kele[1], Tamás A. Martinek[1,2]*

Affiliations:

[1] Department of Medical Chemistry, University of Szeged, Dóm tér 8, H-6720 Szeged, Hungary
[2] MTA-SZTE Biomimetic Systems Research Group, University of Szeged, Dóm tér 8, H-6720 Szeged, Hungary

*Corresponding author. Email: martinek.tamas@med.u-szeged.hu

Table of Contents

Supplementary Text

Dynamic model of chemical evolution for the light-fuelled dissipative system

The mathematical framework of chemical evolution (Kiedrowski and Higgs, references 26 and 27 in the MS) was invoked to analyse the experimentally determined dynamics of the dissipative reaction network. The differential equation describing the time-dependent concentration of the evolving chemical species ([X]) contains three rate terms: non-autocatalytic synthesis (v_s), replication (v_r), and break down (v_b).

$$\frac{d[X]}{dt} = v_s + v_r - v_b \tag{1}$$

Non-autocatalytic synthesis pathways. The spontaneous synthesis of X is possible through radical chain reaction (I). Here, dimers (X) are produced by the reaction between the freely diffusing monomer radicals (M·) and the glutathione-protected monomers (M).

$$M + M^\bullet \xrightarrow{k_{ch}} X + GS^\bullet \tag{I}$$
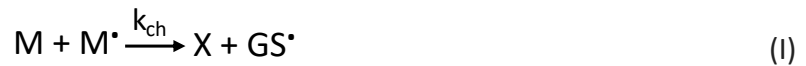
The rate of formation for X in reaction I satisfies equation 2.

$$v_{s,ch} = k_{ch}[M^\bullet][M] \tag{2}$$

The concentration of M· is low and can be approximated with a quasi-steady state approach (eq. 3). Because of the low overall conversion in the experiments, radical M· is produced dominantly by the homolytic cleavage of M. Therefore, the rate of formation is proportional with the light intensity ($k_I I$) and [M]. The chain termination steps consuming M· involve reactions with M· and GS·. Again, the large excess of M affords the approximation that [M·] = [GS·], and thus, the chain termination rate is of second order in [M·].

$$\frac{d[M^\bullet]}{dt} = 0 = k_I I[M] - 2k_t[M^\bullet]^2 \tag{3}$$

$$[M^\bullet] = \sqrt{\frac{k_I I}{4k_t}}[M] \tag{4}$$

Substituting eq. 4 into eq. 2, and substituting the expression with the constants with s_{ch}, the production rate of X through the chain reaction mechanism is given by eq. 5.

$$v_{s,ch} = s_{ch}\sqrt{I}[M]^{1.5} \tag{5}$$

The tendency of the monomers to self-associate renders the radical recombination mechanism (reaction II) a high probability pathway because the diffusion trap effectively lowers the entropic barrier.

$$M + M \underset{}{\overset{K_{DM}}{\rightleftharpoons}} MM \xrightarrow{2\,h\eta} M^\bullet M^\bullet \longrightarrow X \tag{II}$$
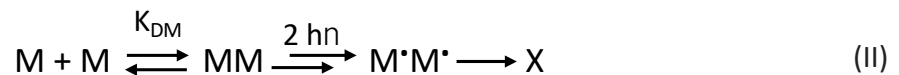
This route is governed by a preequilibrium for the formation of the monomer associates (K_{DM}) and the absorption of two photons during the lifetime of the non-covalent monomer assemblies. The recombination of the radicals within the assembly is a fast asymmetric step without significant energy of activation, because the energy level of the biradical complex is close to the transition state. In this mechanism, M· does not participate in the chain reaction due to the absence of free diffusion. Therefore, the rate of formation is determined by the rate of the light-induced homolytic cleavage of M (eq. 6).

$$v_{s,r} = (k_I I)^2 [MM] \tag{6}$$

Using the preequilibrium relationship to express [MM], and collecting the constant terms into s_r, the rate of the self-association-assisted radical recombination mechanism is given by eq. 7.

$$v_{s,r} = s_r I^2 [M]^2 \tag{7}$$

We assumed that the freely diffusing [M·] is low; consequently, the formation of X *via* diffusion-controlled chain termination by two M· radicals is an unlikely event as compared with the alternative mechanisms. Therefore, it gives a minor contribution to the dimer production, and we neglected this pathway in this approximation.
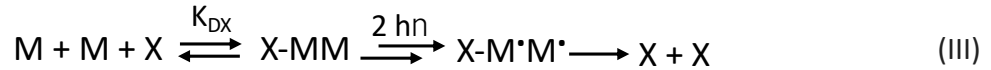
Replication. Experiments strongly suggested positive feedback in the dynamics of formation for X. This can be explained by the presence of an autocatalytic cycle (reaction III), wherein formation of X is self-templated.

$$M + M + X \underset{}{\overset{K_{DX}}{\rightleftharpoons}} X\text{-}MM \xrightarrow{2\ h\eta} X\text{-}M^{\bullet}M^{\bullet} \longrightarrow X + X \tag{III}$$

Following the principles described for the spontaneous synthesis, we assumed that the formation rate is governed by a preequilibrium for the template binding (K_{DX}) and the rate of the light-induced cleavages (eq. 8).

$$v_r = (k_I I)^2 [XMM] \tag{8}$$

We obtain the replication rate (eq. 9) by substituting the equilibrium relationship for the X-MM formation into eq. 8 and collecting the constant terms into r.

$$v_r = r I^2 [X][M]^2 \tag{9}$$

This rate equation is dependent on [X], which is the free dimer available for monomer binding. Our experiments revealed that the steady state total dimer concentration was low micromolar, which is well below the dissociation constant of the dimer-dimer association and the competing monomers were in excess in the solution. Thus, we could neglect the dimer-dimer association-induced product inhibition in the model applied for the pure foldamer mixture.

Breakdown. We do not consider the direct decomposition of X by light absorption (inverse of the last step in reaction II), because the asymmetry of the proximity-controlled radical recombination

was assumed in the first place. A more likely pathway is when X reacts with the glutathione radical ($GS^.$) (reaction IV).

$$X + GS^{\bullet} \xrightarrow{\text{k}_\text{b}} M + M^{\bullet} \tag{IV}$$

The rate equation can be given as follows (eq. 10).

$$v_b = k_b[GS^.][X] \tag{10}$$

To estimate a steady state $[GS^.]$, we can follow similar principles as captured in eqs. 3 and 4. Thus, $[GS^.]$ is proportional with the square root of the light intensity and eq. 2 can be rewritten after substituting the constant terms with the overall rate constant of b (eq. 11).

$$v_b = b\sqrt{I}[X] \tag{11}$$

In this expression, $[X]$ refers to the freely diffusing dimers, of which break down is not inhibited by any association process.

Fitting the dynamic model to the experimental data

After constructing the differential equation for our dissipative chemical evolution system (eq. 12), it was numerically integrated using the Runge-Kutta (RK4) method to simulate the time evolution of a dimer.

$$\frac{d[X]}{dt} = s_{ch}\sqrt{I}[M]^{1.5} + s_r I^2[M]^2 + rI^2[X][M]^2 + b\sqrt{I}[X] \tag{12}$$

$$[M] = [M]_0 - 2[X]$$

The numeric integrations were carried out with the parameters of $[X]_0 = 0$, $[M]_0 = 2\text{x}10^{-5}$ M and $\Delta t = 4.17\text{x}10^{-2}$ h. The light intensities were set to the calibrated values depending on the actual experiment. The rate constants s_{ch}, s_r, r and b were determined by fitting (non-linear regression) the simulated curves against the experimental data points. Importantly, the regression was performed simultaneously for all experiments measured at different light intensities but run with identical initial sample compositions. The non-linear regression resulted in an excellent fit for each sequence. The parameter s_{ch} converged to zero for all sequences studied. This finding indicated that the chain reaction mechanism for the formation of the dimers can be eliminated from the model on the basis of the experimental data, which led to eq. 13.

$$\frac{d[X]}{dt} = s_r I^2([M]_0 - 2[X])^2 + rI^2[X]([M]_0 - 2[X])^2 + b\sqrt{I}[X] \tag{13}$$

Modification of the dynamic model for the protein-templated experiments

Protein-dependent autocatalytic route to dimer formation. As a first approximation, the dynamic model given in eq. 13 was applied to the protein-templated experiments. We expected that the presence of the protein increases the apparent s_r as the results of the catalytic (but not autocatalytic) effects. We found, however, that the simultaneous fit to the experimental data recorded at different light intensities was not possible due to a biexponential behaviour. This effect was prevalent for the sequences that did not correspond to the native recognition motif of the template protein (entirely hydrophobic, not containing any cationic side chain). The results indicated an additional protein-dependent mechanism leading to a non-linear response at the early stage of the time evolution beyond the entirely self-templated replication. We searched for a protein-dependent reaction pathway, where dimer binding introduces positive feedback into the rate equation. Calmodulin is a dumbbell-shaped protein, and a flexible segment connects the domains containing the native binding regions. The protein is, therefore, quasisymmetric. Based on the symmetry and flexibility, we hypothesised that calmodulin could sequentially bind two dimers if dimers are in excess relative to the target. The assumed binding mode was confirmed by ITC measurements (Supplementary Fig. 5). This arrangement suggests an additional route in a retrosynthetic approach, where a monomer displaces a dimer segment on one of the protein domains, and an additional monomer binds to the displaced foldamer segment (Supplementary Fig. 4). This way, the complex can colocalise two monomers to catalyse dimer formation. This protein-dependent autocatalytic pathway is captured in reaction V.

$$M + M + PX \underset{}{\overset{K_{PXM}}{\rightleftharpoons}} PX\text{-}MM \xrightarrow{2\ h\nu} PX\text{-}M^\bullet M^\bullet \longrightarrow PX + X \qquad (V)$$
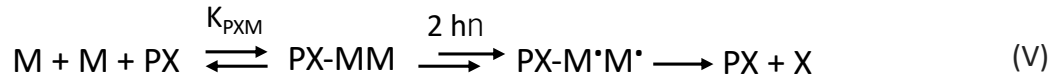
First, we solved the preequilibrium for the formation of the dimer-protein complex PX with the help of the mass balances (eq. 14). $[P]_t$ and $[X]_f$ stand for the total protein and the non-bound dimer concentrations. We note that the dissociation constant K_{PX} is an apparent value in this case because of the implicit displacement effect of the monomers.

$$K_{PX} = \frac{[X]_f [P]}{[PX]} \qquad (14)$$

$$[P]_t = [PX] + [P], \qquad [X] = [X]_f + [PX]$$

Solving the quadratic equation system 14 for [PX] and selecting the realistic solution yields eq. 15.

$$[PX] = \frac{1}{2}(K_{PX} + [P]_t + [X]) - \sqrt{(K_{PX} + [P]_t + [X])^2 - 4[X][P]_t} \qquad (15)$$

We can substitute the preequilibrium concentration of PX (eq. 15) into the rate equation written up for reaction V (eq. 16).

$$v_{s,PX} = s_{PX} I^2 [PX][M]^2 \qquad (16)$$

7

Adding this rate term to the total dynamic model allowed the correct simulation of the initial slopes and the steady state concentrations within a single theoretical framework for all light intensities. Parameters K_{PX} and $[P]_t$ were introduced as additional sequence-specific fitted variables in the regression.

Inhibition effects of the dimer-dimer association on the replication and breakdown.
For the protein-templated samples, we observed that the simulated curves at the highest light intensity steeply approach the steady state level, which led to a minor deviation from the experimental observations. We assumed that the flatter curvature is due to a dimer concentration-dependent product inhibition affecting both replication and breakdown rates. The plausible explanation for such an effect was the dimer-dimer association, which cannot be neglected above the total dimer concentration of ca. 5 µM produced in the protein-templated samples. The protein – dimer affinity is magnitudes higher than that of the dimer-dimer interaction, which allowed separate handling of the self-association equilibrium (eq. 17).

$$K_{XX} = \frac{[X]_f^2}{[X_2]} \tag{17}$$

Experimental data supported that dimer-dimer interaction had only a minor influence on the replication and the breakdown rates. On this ground, we can conclude that $[X_2] << [X]_f$ and $[X_2]$ can be expressed as a function of $[X]_f$ (eq. 18).

$$[X_2] = \frac{1}{K_{XX}} [X]_f^2 \tag{18}$$

Substituting eq. 18 into the mass balance yields the corrected free dimer concentration ($[X]_f^{'}$) in eq. 19.

$$[X]_f' = [X]_f \left(1 - \frac{[X]_f}{K_{XX}}\right) \tag{19}$$

After substituting eq. 19 into eq. 13, the simulated curves displayed an improved agreement with the experimental data. Parameter K_{XX} was introduced as an additional fitted variable in the regression.

Light intensity dependence of the dimer concentration in the steady state

In the stationary state, the time derivative of the dimer concentration is zero. This behaviour allowed an algebraic formula for the time-invariant $[X]$ starting from eq. (eq. 13).

$$[X] = \frac{sM^2I^{1.5}}{b - rM^2I^{1.5}} \tag{20}$$

Here, we neglected the monomer depletion (at low conversion) to focus on the effect of the light intensity. This way, we obtained a hyperbolic relationship between the steady state dimer concentration and the light intensity, which is valid in the low conversion regime. The hyperbolic dependence on the light intensity yield a switch-like response in the concentration of the

8

replicating dimers as the light intensity exceeds a certain level. This behaviour is in excellent agreement with our experimental data.

ITC characterisation of the binding of foldameric dimers to CaM

To quantitatively characterise the interaction between the foldameric dimers and the seeding protein, two of the best ligands (**WF-RW** and **WW-RF**) were selected as representatives from the dissipative selection experiment. Fragments of the dimers were coupled together through a chemically stable thioether linkage (referred to as **WF-S-RW** and **WW-S-RF**). Both dimers displayed two-step binding to CaM (Supplementary Fig. 5). First, a high-affinity step was found with a K_D of 1.76 ± 0.65 nM (n = 1.02 ± 0.03) for **WF-S-RW** and 8.74 ± 4.03 nM (n = 1.01 ± 0.05) for **WW-S-RF**. The 1:1 stoichiometry in both cases strongly suggested that the two lobes of the protein with separate binding sites were involved in the binding of a single foldameric dimer. Second, a lower affinity step with fractional stoichiometry was also detected for both dimers (Supplementary Fig. 5a and 5c). This finding supported that the protein can bind two dimers simultaneously in excess of the ligand. In order to confirm that the foldameric ligands recognise the orthosteric interface of the template, competitive ITC experiment was carried out with TRPV1-CT_{15}, the native ligand of CaM, as described previously (*1*). CaM: foldameric dimer 1:2 sample was titrated with TRPV1-CT_{15} during which no binding events were found (Supplementary Fig. 5)

Supplementary Methods

Synthesis and purification of the foldameric sequences

Foldameric sequences having L-Gly-L-Gly-L-Cys C-terminal segments were synthesised manually using standard solid-phase peptide synthesis with Fmoc/tBu chemistry. Rink Amide AM resin was used as solid support (capacity: 0.71 mmol/g) and HATU (1-[bis(dimethylamino)methylene]-1*H*-1,2,3-triazolo[4,5-b]pyridinium 3-oxid hexafluorophosphate) as coupling reagent in the presence of DIEA (*N,N*-diisopropylethylamine). Amino acids and coupling reagents were used in excess of 3 equivalents and shaking was applied at room temperature for 3 h. Deprotection was carried out with a DMF (*N,N*-dimethylformamide) solution containing 2% DBU (1,8-diazabicycloundec-7-ene) and 2% piperidine. Cleavage was performed with TFA/H_2O/DTT (DL-dithiothreitol)/TIS (triisopropylsilane) (90:5:2.5:2.5), which was followed by precipitation in ice-cold diethyl ether. The resin was washed with acetic acid and water, filtered, then lyophilised. Peptides were purified by RP-HPLC on a C18 column (Phenomenex Luna C18, 250 x 10.00 mm, particle size: 10 μm, pore size: 100 Å). The HPLC eluents were 0.1% TFA in water (Eluent A), and 0.1% TFA/ 80% ACN (acetonitrile) in water (Eluent B). Different gradient elution was used according to the hydrophobicity of the peptides. Purity was confirmed by analytical RP-HPLC and ESI-MS measurements.

Synthesis and purification of the foldamer-glutathione adducts

Disulphide precursors were synthesised by oxidative coupling of thiols in the solution phase. Each purified foldamer was dissolved in 20% DMSO (dimethyl sulfoxide) in water separately to 1 mM

concentration in the presence of 20 times molar excess of GSH (reduced glutathione) and stirred overnight at room temperature exposed to atmospheric oxygen. The completeness of the oxidation reaction was monitored by HPLC-MS, and the reaction mixture was injected directly onto a semi-preparative HPLC column (Phenomenex Luna C18, 250 x 10.00 mm, particle size: 10 μm, pore size: 100 Å) and purified. Under this reaction condition the amount of the homodimeric foldamer was negligible and could be completely separated from the foldamer-glutathione adduct.

Synthesis and purification of WF-S-RW and WW-S-RF dimers with thioether linkage

Chloroacetylated RW and RF fragments were synthesised on a solid support using Fmoc/tBu chemistry. Fmoc-L-Lys(Mtt)-OH was coupled first to the C-terminal of the peptide and Boc-protected 1S,2S-ACHC-OH was coupled to the last amino acid at the N-terminus of the peptide. Without the cleavage of the Boc-protecting group, the Mtt (4-methyltrityl) protecting group was cleaved by washing the resin with TFA/DCM (1:99) for 1-2 minutes and this procedure was repeated until the filtrate was not yellow anymore. Prior to coupling, the resin was neutralised with 5% DIEA in DMF. Free ε-amino group of Lys was chloroacetylated by coupling 5 equivalents of chloroacetic anhydride in the presence of 5 equivalents of DIEA. The crude peptides (RW-Lys(ClAc) and RF-Lys(ClAc)) were cleaved from the resin with a mixture of TFA/H_2O/TIS (92:5:3) and followed by precipitation in ice-cold diethyl ether. The resin was washed with concentrated acetic acid, acetonitrile and water, then filtered and lyophilised. Crude peptide was purified by RP-HPLC on a C18 column (Phenomenex Luna C18, 250 x 10.00 mm, particle size: 10 μm, pore size: 100 Å). The purified **RW-Lys(ClAc)** and **RF-Lys(ClAc)** peptides were completely dissolved in 0.1 M Tris buffer (pH 8.2) with DMF as a co-solvent. Previously purified thiol functionalised fragment (**WF-SH** and **WW-SH**, respectively) was dissolved in the same buffer in 1.5 molar excess and added to the appropriate chloroacetylated fragment under continuous stirring. After overnight incubation at room temperature, the mixture was injected directly onto a C18 HPLC-column and purified. Purity was confirmed by analytical RP-HPLC and ESI-MS measurements.

CaM expression and purification

Calmodulin (CaM) (bovine) gene was cloned into pET28a vector. The sequenced plasmid was then transformed to competent *E. coli* cells (BL21 DE3) for protein expression. Cells were grown on LB liquid media at 37°C until OD600 = 0.5, then expression of CaM was induced by adding 200 μM IPTG and was carried out overnight (~19 hours) at 22°C. After centrifugation, cell pellets were resuspended in Ni-NTA Lysis Buffer (50 mM NaH_2PO_4, 300 mM NaCl, 10 mM imidazole, pH 8.0) and were lysed by sonication with addition of 1 μM Leupeptin, 0.1 μg ml^{-1} Pepstatin A and 20 μM PMSF (Phenylmethylsulfonyl fluoride). The cleared lysate was first purified using a Ni-NTA filled column according to the manufacturer's protocol (Expression and purification of proteins using 6×Histidine-tag): After equilibration of the Ni-NTA column, lysate was added for a short incubation on ice (30 minutes), washed with Ni-NTA Wash Buffer (50 mM NaH_2PO_4, 300 mM NaCl, 20 mM imidazole, pH 8.0), and finally CaM was eluted with small volumes of Ni-NTA Elution buffer (50 mM NaH_2PO_4, 300 mM NaCl, 250 mM imidazole, pH 8.0).The clear fractions were concentrated using Amicon Ultra Filter Device (10K) and the buffer was changed to 20 mM HEPES, pH 7.0. The His-tag was removed with an overnight Thrombin digestion at 4 °C leaving 9 extra amino acid (GSHMARSNS) on the N terminus of the protein. Thus, the molecular weight

of the protein was 17765.58 g mol^{-1}, which was confirmed by ESI-MS measurements. In order to remove additional cleavage fragments after thrombin treatment CaM was purified by using RP-HPLC on a C4 column (Phenomenex, Jupiter 250x10 mm), using the following gradient elution: 40-70% Eluent B over 60 minutes at 4 ml min^{-1} flow rate with A: 0.1% TFA in water and B: 0.1% TFA/80% ACN in water. After lyophilisation, the protein was subjected to dialysis in 20 mM, pH 7.0 HEPES buffer in order to remove TFA traces and ensure correct folding. Purity and folding was assessed by HPLC-MS, native ESI-MS and NMR measurements. CaM concentration was measured by using BCA assay (Thermo Scientific, Pierce) utilising the manufacturer's protocol.

Conversion of measured AUC to concentration

Statistical product distribution of the foldameric building blocks were generated from the 12-membered glutathione-protected foldameric library. The library was dissolved in 20% DMSO in water each one at 10 µM concentration, and library members were reduced with 2 molar equivalents of TCEP (tris(2-carboxyethyl)phosphine) followed by continuous stirring for 48 h. Completeness of reoxidation was monitored by HPLC-MS and final product distribution was analysed by the same method as the UV-induced experimental samples. Expected concentration of each building block was calculated based on the uniform distribution of the compounds. After the quantitative evaluation of the chromatograms, the AUC/concentration ratios were defined for each library member (Supplementary Table 9).

Testing the sensitivity of CaM to UV irradiation

CaM in a concentration of 6 µM was irradiated with UV light (365 nm, 5.1 mW cm^{-2}) for 11 h under argon atmosphere, and samples were taken in every hour to monitor the stability of the protein. Samples were measured directly with HPLC-MS technique. Besides the intact protein (CaM, 17765.1992 Da) the mass of the oxidised protein was detectable, expected to be Met-oxidised products after 5 h of irradiation (Supplementary Fig. 2). In order to identify the affected Met residues, the samples were analysed via HPLC-MS/MS after enzymatic digestion (Trypsin protease) of the protein. List of the resulting peptidic fragment sequences with their calculated mass was generated with ProteinProspector v 6.2.1 MS-Digest webpage (University of California, San Francisco, CA, USA). The presence and intensity of the oxidised fragments were characterised with the area under the curve (AUC) values and expressed in relative % to the intact protein fragment (Supplementary Table 8). The 95% of the protein remained intact after 5 h irradiation. The residue Met[119] was most affected, of which 4.8% was oxidised after 5 h UV irradiation. Met[119] has a minor effect on ligand binding (2).
Sequence of CaM (calculated MW= 17765.43 g mol^{-1}):
GSHM[4]ARSNSM[10]ADQLTEEQIAEFKEAFSLFDKDGDGTITTKELGTVM[46]RSLGQNPTEA ELQDM[61]INEVDADGNGTIDFPEFLTM[81]M[82]ARKM[86]KDTDSEEEIREAFRVFDKDGNGYIS AAELRHVM[119]TNLGEKLTDEEVDEM[134]IREADIDGDGQVNYEEFVQM[154]M[155]TAK

Proteomic analysis of the oxidised CaM samples

After enzymatic digestion the product composition was analysed with UHPLC-MS/MS measurements using an ACQUITY I-Class UPLC™ liquid chromatography system (Waters, Manchester, UK) coupled with a Q Exactive™ Plus Hybrid Quadrupole-Orbitrap Mass Spectrometer (Thermo Fisher Scientific, San Jose, CA, USA). Chromatographic separation was carried out at 25 °C using 0.1% formic acid in water as solvent A and ACN containing 0.1% formic acid as solvent B. The following multistep gradient was used: 5-50% over 20 minutes then 50-80% over 5 minutes and finally 80% solvent B for additional 5 minutes at 0.7 mL min^{-1} flow rate. Samples where incubated at 5°C until the measurement and 15 µL of the sample was injected into the UHPLC–MS/MS system. The MS instrument was operated in the positive-ion mode using the equipped HESI-II source with the following parameters: capillary temperature: 256°C; spray voltage: 3.5 kV; aux gas heater temperature: 412°C; sheath gas flow: 47.5 mL min^{-1}; aux gas flow: 11 mL min^{-1}; and S-lens RF level, 50.0 (source auto-defaults). Full scan was conducted with a mass range of 150–2000 m/z with resolution of 70,000. The ACG (automatic gain control) setting was defined as 3×10^6 charges, and the maximum injection time was set to 100 ms. Data dependent MS/MS was acquired in a mass range of 200-2000 m/z with resolution of 17,500. AGC setting was defined as 5×10^5 charges, and the maximum injection time was set to 150 ms.

Isothermal titration calorimetry (ITC) experiments

ITC experiments were carried out with a MicroCal™ VP-ITC microcalorimeter (GE Healthcare, Northampton, MA, USA). **WF-S-RW** (MW: 2151.26 g mol^{-1}) and **WW-S-RF** (MW: 2151.26 g mol^{-1}) conjugates were dissolved in 20 mM HEPES, 150 mM NaCl, 5 mM CaCl$_2$ pH=7.4 buffer and they were sonicated for 20 minutes before titration to avoid aggregation. Foldamer solution (15 µl) was injected from the computer-controlled microsyringe into the CaM solution at intervals of 240 s. Concentration of CaM in the cell was 3 µM, and the concentration of foldamers in the syringe was 75-80 µM. The temperature was adjusted to 303 K. The control experiments were performed by injecting foldamers into the cell containing buffer with no target. Experiments were repeated twice. The experimental data were fitted to the two independent sites model (adjustable parameters: ΔH_{b1}, K_{d1}, n_1 and ΔH_{b2}, K_{d2}, n_2) using a nonlinear least-squares procedure. Errors were calculated via jackknife resampling.

Calculation of the amplification factors and the Shannon diversity indices

Amplification factors (AF) were calculated for each dimer to indicate the enrichment of the compounds. The following formulas (eqs. 21 and 22) were used to calculate the amplification as a result of light intensity increase:

$$AF_{i(C),int} = \frac{AUC_{i(C),100\%}}{AUC_{i(C),50\%}} \tag{21}$$

where $AUC_{i(C),100\%}$ is the area under the curve (AUC) of compound i measured at 100% light intensity (5.10 mW cm^{-2}) and $AUC_{i(C),50\%}$ is the AUC of the same compound measured at 50% light intensity (2.55 mW cm^{-2}). Both are measured in the pure foldameric system.

$$AF_{i(P),int} = \frac{AUC_{i(P),100\%}}{AUC_{i(P),50\%}} \tag{22}$$

where $AUC_{i(P),100\%}$ is the area under the curve (AUC) of compound i measured at 100% light intensity (5.10 mW cm^{-2}) and $AUC_{i(P),50\%}$ is the AUC of the same compound measured at 50% light intensity (2.55 mW cm^{-2}). Both are measured in the protein-templated sample.

Eq. 23 was used to directly express the effect of protein template on amplification of the dimers.

$$AF_{i,prot} = \frac{AUC_{i,prot}}{AUC_{i,control}} \tag{23}$$

where $AUC_{i,prot}$ is the area under the curve (AUC) of compound i in the protein-templated sample and $AUC_{i,control}$ is the AUC of the same compound in the absence of the protein.

Calculation of experimental error. Errors of AF_i (σ_{AF}) were calculated from three parallel measurements, by using the following general formula (neglecting the correlation between the variables):

$$\sigma_{AFi} = AF_i \sqrt{\left(\frac{\sigma_{AUC1}}{AUC_1}\right)^2 + \left(\frac{\sigma_{AUC2}}{AUC_2}\right)^2} \tag{24}$$

where $AUC_1 \pm \sigma_{AUC1}$ and $AUC_2 \pm \sigma_{AUC2}$ are the measured variables with uncertainties when AF_i is calculated by AUC_1/AUC_2.

Calculation of Shannon diversity indices. Shannon diversity index (I_{Sh}) was calculated for the sets of amplification values obtained under different conditions.

$$I_{Sh} = -\sum_{i=1}^{n} p_i \times \ln p_i \tag{25}$$

Here, p_i is the probability of amplification for the ith component approximated by the normalised amplification factors. As a proxy for the selection efficiency, the diversity decrease (ΔI_{Sh}) was calculated relative to a theoretical maximum diversity case, where all amplification was uniform (I_{Sh}^{max}).

$$\Delta I_{Sh} = I_{Sh} - I_{Sh}^{max} \tag{26}$$

Calculation of the side chain enrichment

Enrichment (E) of the proteinogenic side chains in the peripheral (1, 1') and the central (2, 2') positions of the ten most amplified dimers was expressed as the frequency of a side chain relative to all side chains in the foldamer system by using the following formula:

$$E_{schi} = \frac{N_{schi,Best}/10}{N_{schi,All}/78} \tag{27}$$

Where E_{schi} is the enrichment of the side chain i in appropriate position, $N_{schi,Best}$ is the count of the side chain i among the top ten amplified dimers, $N_{schi,All}$ is the count of the side chain i in the complete system.

Supplementary Figures
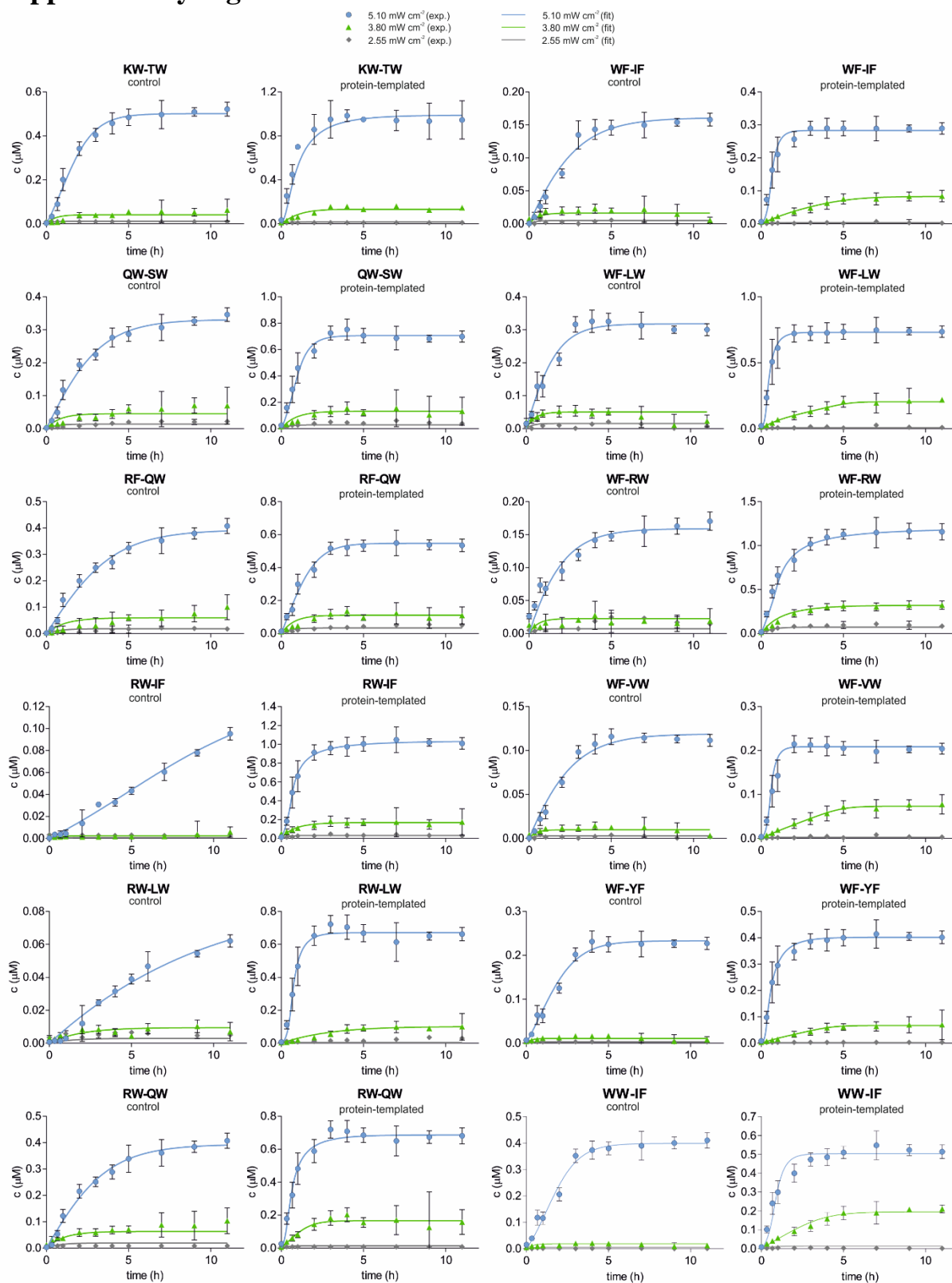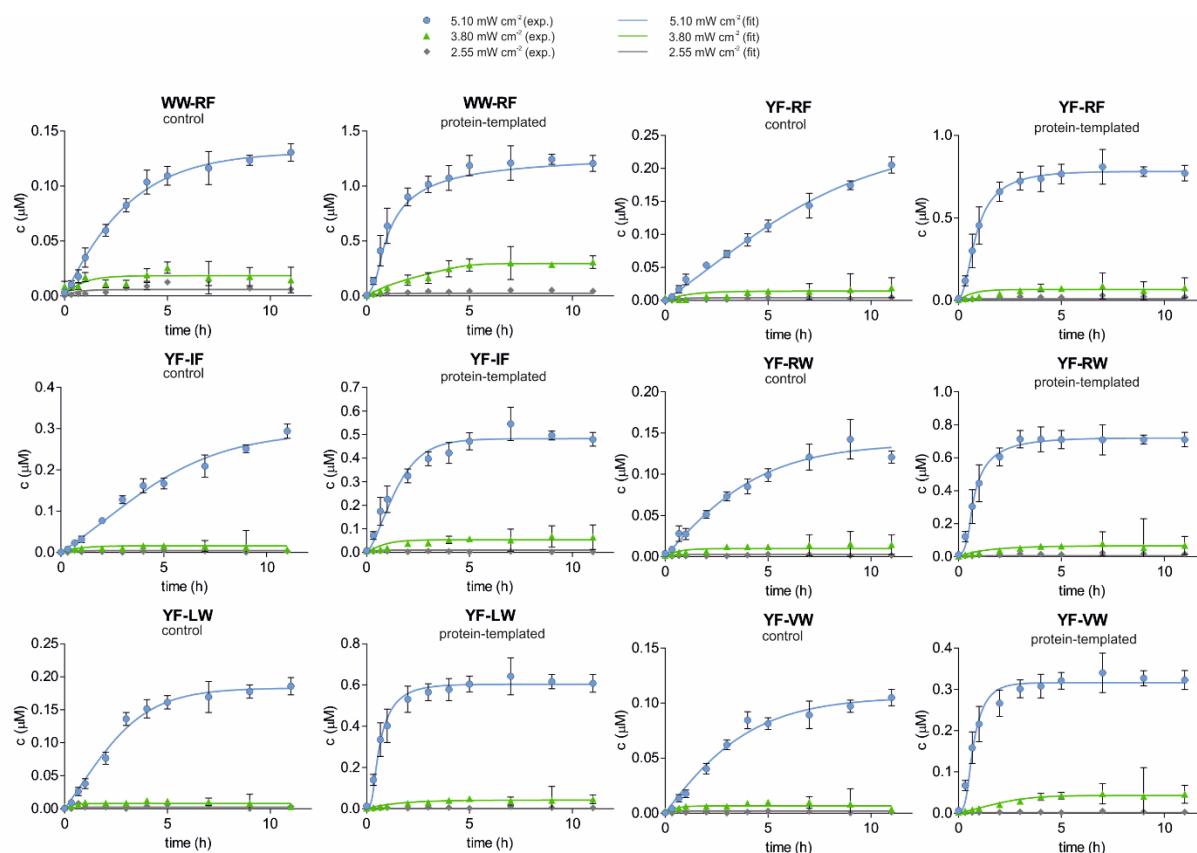
Supplementary Figure 1. Fitting of the dynamic model of chemical evolution to experimental data for representative replicators. Replicator concentration vs. time measured for the pure foldamer system ('control') and for the protein-templated system ('protein-templated'). Data at different light intensities are represented as follows: 2.55 mW cm^{-2} (gray diamond), 3.80 mW cm^{-2} (green triangle), 5.10 mW cm^{-2} (blue circle); fitted curves are depicted with matching color. Non-linear least square analysis was used for fitting. Experimental data were obtained from three parallel measurements carried out on three different samples. See Supplementary Tables 2-3 for fitted parameters.
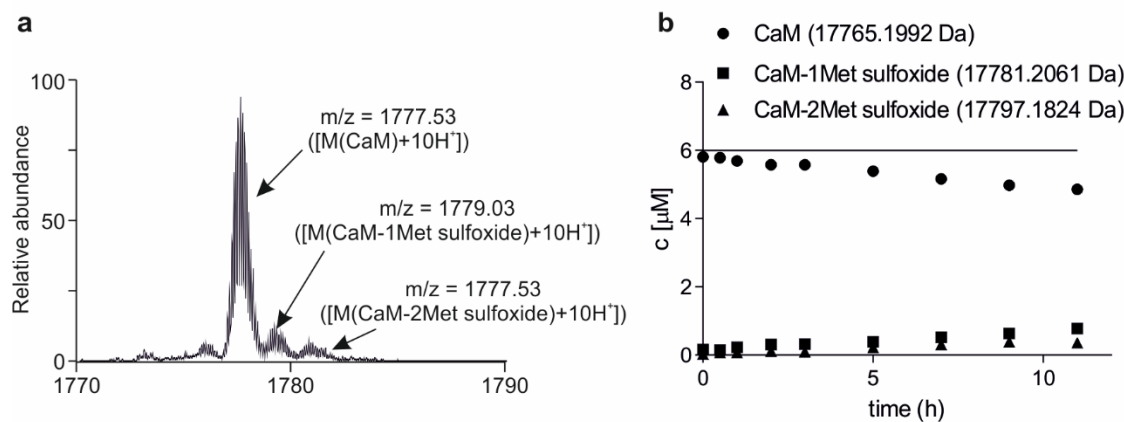
Supplementary Figure 2. Monitoring the UV-induced degradation of CaM. CaM at a concentration of 6 μM was irradiated with UV light (365 nm, 5.1 mW cm^{-2}) for 11 h (**a**) extracted

MS spectrum of CaM after 5 h irradiation showed appearance of oxidised protein, (**b**) time dependence of the concentration of the intact CaM (circle) and the oxidised species (square and triangle).
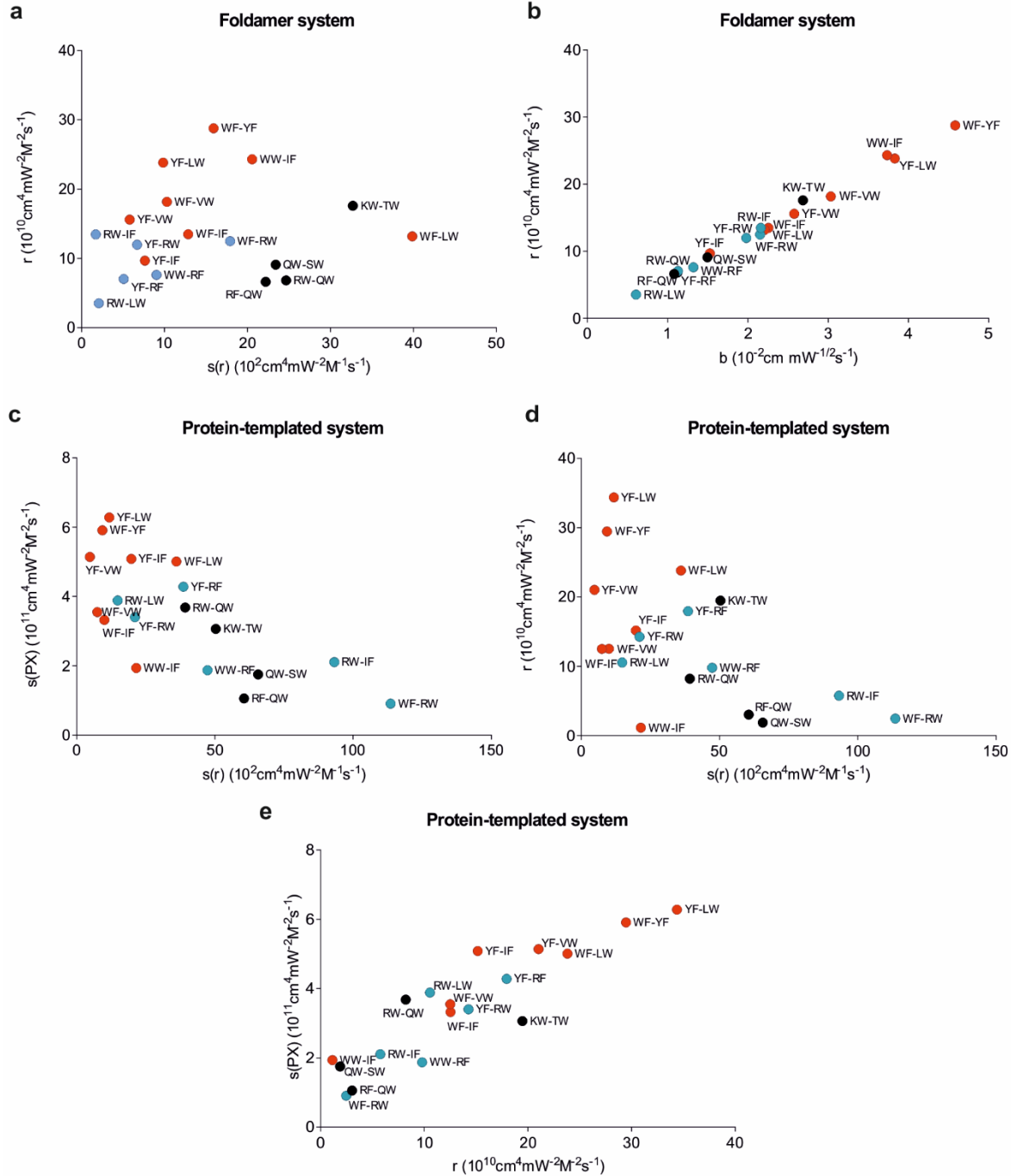
Supplementary Figure 3. Relationship between the fitted rate constants. Correlation depicted for the representative set of foldamers: *s(r)* is the rate constant for the spontaneous dimer formation *via* direct radical recombination, *s(PX)* is the rate constant for the protein-dependent autocatalytic dimer synthesis, *r* is the rate constant for the template-directed replication and *b* is the rate constant

for the chain reaction-mediated breakdown of the dimers. Replicators having similar chemical characteristics are labelled with the same color code: hydrophobic/aromatic side chains in all variable positions (red); one positively charged side chain in the sequence (blue); two polar side chains in the sequence (black).
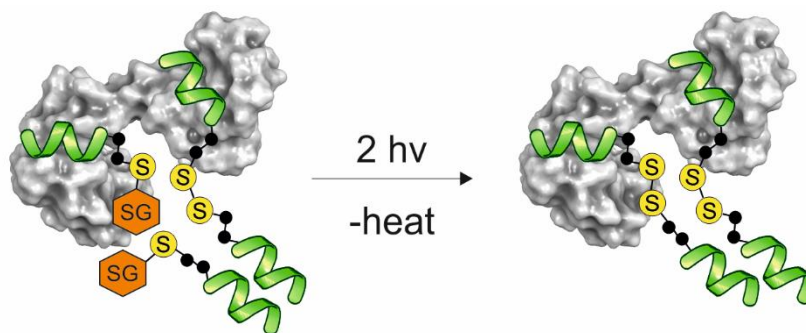
Supplementary Figure 4. Schematic representation of the protein-dependent autocatalytic pathway. A monomer can displace one of the dimer segments on one of the protein domains allowing an additional monomer to bind to the displaced foldamer segment. ITC data confirmed the existence of the 2:1 replicator:protein complex.
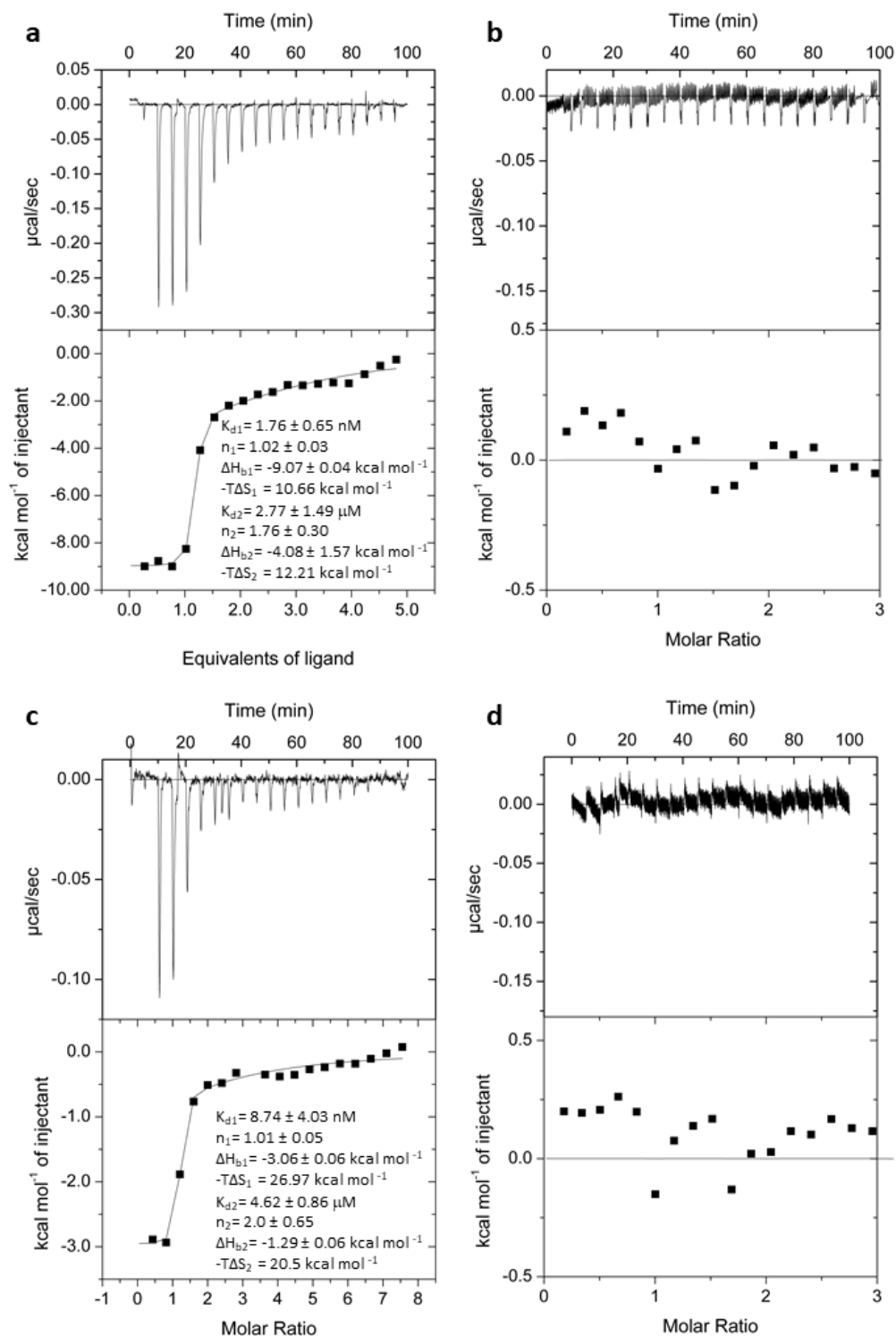
Supplementary Figure 5. Competitive and control ITC titrations for WF-S-RW and WW-S-RF ligands. Raw data (upper) and integrated peaks with fitted values (lower) with Kd, stoichiometry and thermodynamic parameters of the binding. (**a**) **WF-S-RW** titrated to 3 µM CaM in the cell; (**b**) TRPV1-CT$_{15}$ titrated to CaM:**WF-S-RW** 1:2 sample; (**c**) **WW-S-RF** titrated to 3

µM CaM in the cell; (**d**) TRPV1-CT$_{15}$ titrated to CaM:**WW-S-RF** 1:2 sample. All titrations were performed in pH 7.4 20 mM HEPES buffer, 150 mM NaCl with 5 mM CaCl$_2$, at 303 K.
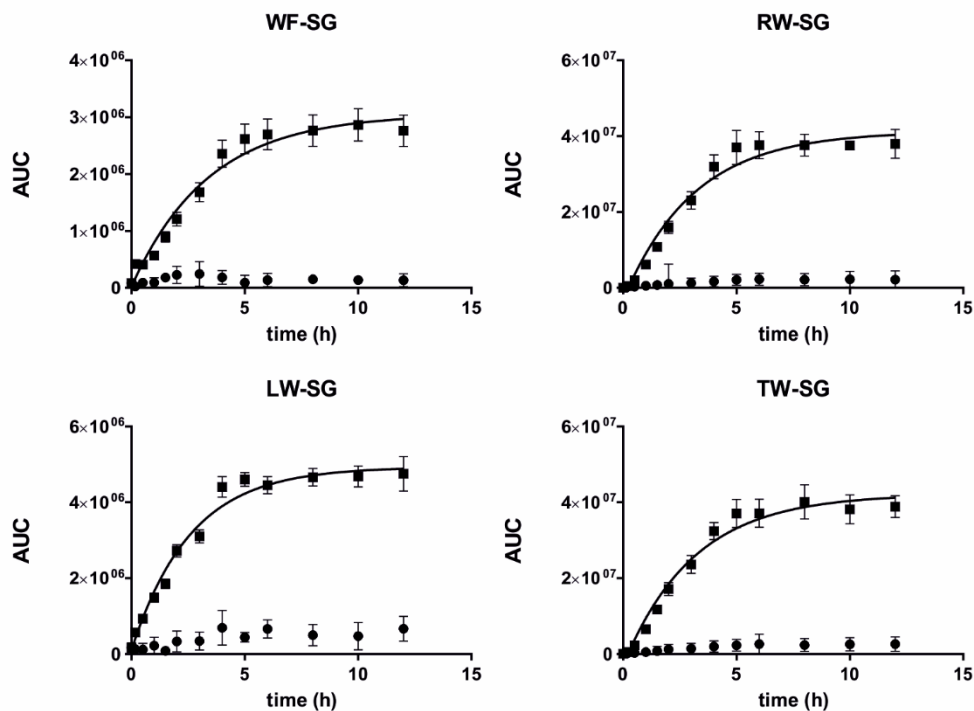
Supplementary Figure 6. Testing the effect of UV light in the disulphide rearrangement. Monitoring the amount of the glutathione adducts starting from foldameric dimers in the presence of GSSG (oxidised glutathione) with UV irradiation (square) and without UV irradiation (circle).
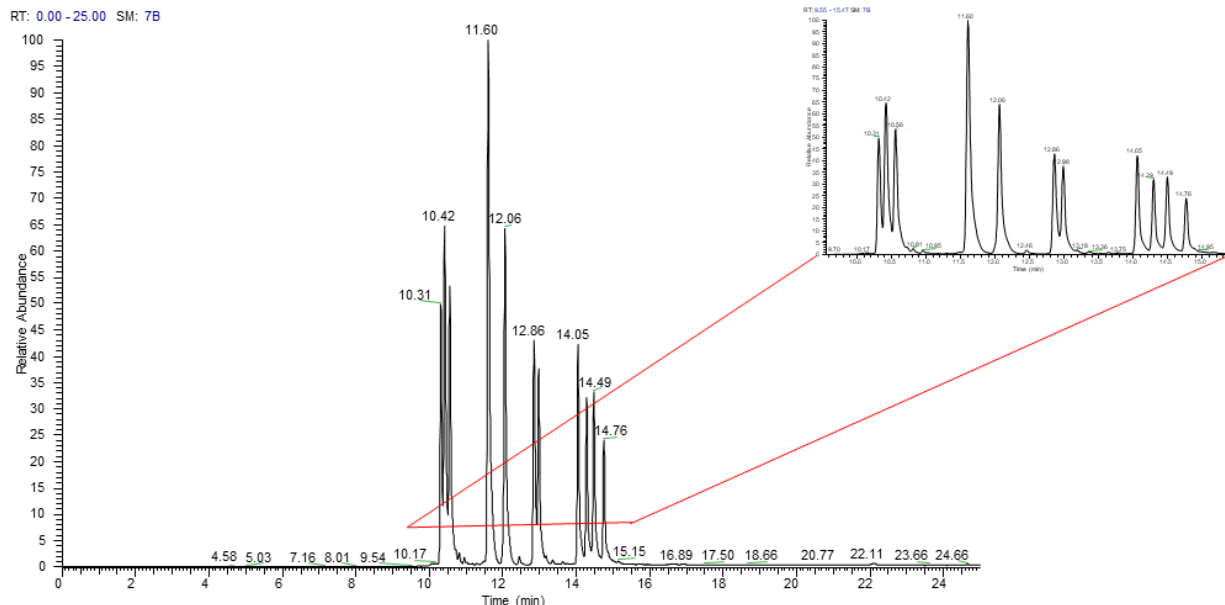
Supplementary Figure 7. Characterisation of the monomer library. Total ion chromatogram of the initial foldamer library containing 12 different glutathion-protected monomers. Conditions of the analytical HPLC-MS measurement: Column: Aeris Widepore XB-C18 (250 x 4.6 mm) Method: 5-80% B during 25 minutes, flow rate: 0.7 mL min^{-1}, where eluent A: 0.1% HCOOH in water, eluent B: 0.1% HCOOH in ACN. For retention time and molar mass of the compounds see Supplementary Table 8.
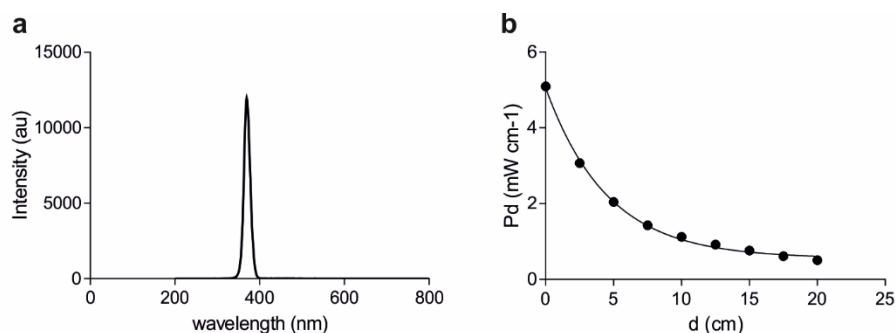
Supplementary Figure 8. Calibration of the UV light source. (**a**) emission spectrum of the UV light source (UVL-28 EL Series UV Lamp), with an emission maximum of 365 ± 5 nm and (**b**) dependency of the power density on the distance measured with S140C Integrating Sphere Photodiode Power Sensors (Thorlab Inc.), wavelength range of the Si detector: 350-1100 nm, Power range: 1 µM-500 mW (Resolution: 1 nW)
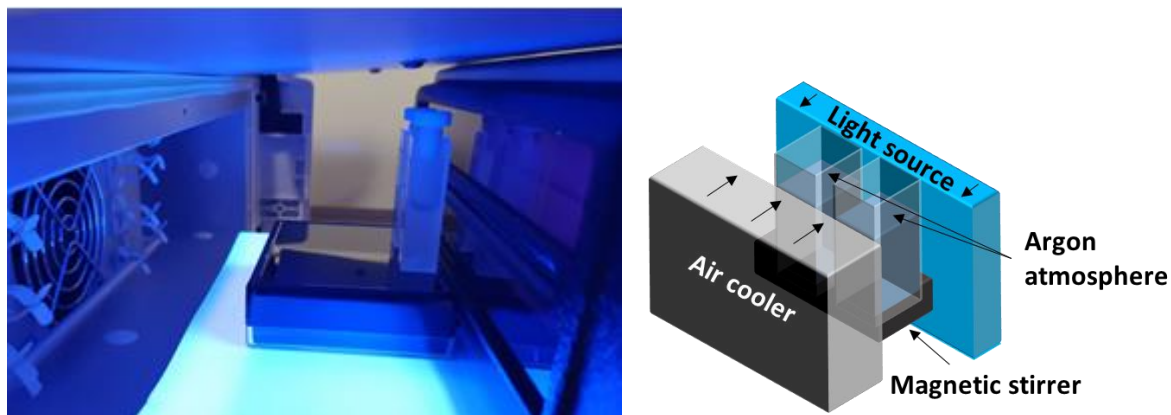
Supplementary Figure 9. Photo and schematic representation of the experimental setup. The reaction mixtures were stirred at 150 RPM in quartz cuvettes having PTFE stopper and kept under argon atmosphere during the experiment. Constant temperature, 303 ± 1 K was maintained *via* active air cooling system (column thermostat). Temperature was monitored with laser gun thermometer. Continuous irradiation of the samples was carried out by UVL-28 EL Series UV Lamp working at 365 nm (Analytic Jena US, Upland, CA) and the power density was varied by increasing the distance between the light source and the samples.

Supplementary Tables

Supplementary Table 1. Characterisation of the foldameric building blocks

Compounds	Calculated molar mass (Da)	Retention time (min)*	Detected ions	
			$[M+2H^+]^{2+}$	$[M+3H^+]^{3+}$
IF-IF	2044.66	17.73	1022.95	682.29
IF-QW	2098.67	15.70	1049.79	700.47
IF-SG	1327.62	14.49	664.84	443.54
IF-SW	2057.62	15.79	1029.89	686.75
IF-TW	2071.65	16.05	1036.42	691.59
IF-VW	2069.67	17.29	1035.41	690.82
KW-IF	2098.71	14.55	1049.79	700.00
KW-KW	2152.76	11.70	1077.40	718.48
KW-LW	2137.75	14.70	1069.44	713.56
KW-QW	2152.72	12.73	1076.93	718.90
KW-RF	2141.74	11.63	1071.41	714.82
KW-SG	1381.69	10.42	691.85	461.56
KW-SW	2111.63	12.73	1056.87	705.04
KW-TW	2125.70	13.09	1063.35	709.34
KW-VW	2123.68	14.26	1063.34	708.73
LW-IF	2084.61	17.84	1042.52	695.41
LW-LW	2123.72	18.00	1062.03	708.28
LW-QW	2137.71	15.84	1069.41	713.77
LW-SG	1366.68	14.76	684.35	456.56
LW-SW	2096.66	15.94	1048.90	700.19
LW-TW	2111.67	16.19	1056.01	704.69
LW-VW	2108.71	17.43	1054.60	703.40
QW-QW	2152.68	13.71	1077.12	718.79
QW-SG	1381.65	11.60	691.83	461.55
RF-IF	2087.69	14.59	1044.38	697.05
RF-LW	2126.73	14.77	1063.94	709.58
RF-QW	2141.70	12.73	1071.37	715.15
RF-RF	2130.72	11.64	1066.67	710.97
RF-SG	1370.68	10.31	686.35	457.89
RF-SW	2100.65	12.80	1050.89	701.43
RF-TW	2114.68	12.77	1057.93	706.26
RF-VW	2112.70	14.28	1056.99	705.03
RW-IF	2126.73	14.77	1064.57	709.87
RW-KW	2180.78	11.80	1091.33	728.04
RW-LW	2165.77	14.91	1083.50	722.76
RW-QW	2180.74	12.90	1090.87	728.20
RW-RF	2169.76	12.22	1085.36	724.15
RW-RW	2208.80	11.97	1104.90	737.47

RW-SG	1409.69	10.56	705.85	470.90
RW-SW	2139.69	12.96	1070.38	714.39
RW-TW	2153.72	13.29	1077.46	718.90
RW-VW	2151.74	14.41	1076.35	718.45
SW-QW	2110.69	13.76	1056.41	704.63
SW-SG	1340.63	11.60	671.32	447.88
SW-SW	2070.58	12.99	1035.86	690.84
TW-QW	2125.66	14.05	1063.25	709.33
TW-SG	1354.64	12.06	678.33	452.55
TW-SW	2083.70	14.13	1042.93	695.92
TW-TW	2098.64	14.35	1049.99	700.56
VW-QW	2122.74	15.35	1063.00	708.79
VW-SG	1352.66	14.05	677.34	451.89
VW-SW	2082.63	15.44	1042.40	695.14
VW-TW	2096.66	15.70	1049.37	699.79
VW-VW	2094.68	16.97	1048.03	698.88
WF-IF	2117.72	17.27	1059.49	706.71
WF-KW	2171.77	14.31	1086.48	724.64
WF-LW	2156.76	17.45	1078.90	719.64
WF-QW	2171.73	15.40	1086.93	724.91
WF-RF	2160.75	14.37	1081.34	721.03
WF-RW	2199.79	14.48	1100.43	734.51
WF-SG	1400.66	14.29	701.34	467.89
WF-SW	2130.68	15.49	1065.95	711.30
WF-TW	2144.71	15.76	1073.20	715.93
WF-VW	2142.73	16.96	1071.97	715.50
WF-WF	2190.78	16.96	1095.93	731.76
WF-WW	2229.81	16.41	1115.44	744.44
WF-YF	2167.74	16.10	1084.52	723.76
WW-IF	2156.75	16.78	1078.99	719.84
WW-KW	2210.80	13.73	1105.93	738.15
WW-LW	2195.79	16.89	1098.46	732.71
WW-QW	2210.76	14.71	1105.98	737.87
WW-RF	2199.78	14.48	1100.43	734.51
WW-RW	2238.82	13.94	1120.36	747.47
WW-SG	1439.67	12.86	720.84	480.89
WW-SW	2169.71	16.08	1086.53	725.38
WW-TW	2183.74	15.09	1092.55	728.13
WW-VW	2181.76	16.39	1091.41	728.06
WW-WW	2268.84	15.81	1135.45	757.47
WW-YF	2206.77	15.53	1103.89	736.72
YF-IF	2094.68	16.41	1047.94	699.11
YF-KW	2148.73	13.54	1075.00	717.42
YF-LW	2133.72	16.57	1067.86	712.64
YF-QW	2148.69	14.50	1074.93	717.02

YF-RF	2137.71	13.54	1069.47	713.51
YF-RW	2176.75	13.71	1088.93	726.82
YF-SG	1377.66	12.98	689.83	460.22
YF-SW	2107.64	14.58	1054.34	703.55
YF-TW	2121.67	14.84	1061.45	707.98
YF-VW	2119.69	16.06	1060.47	707.47
YF-YF	2144.70	15.22	1073.30	715.89

*Analytical HPLC-MS measurement. Column: Aeris Widepore XB-C18 (250 x 4.6 mm) Method: 5-80% B during 25 min, flow rate: 0.7 mL/min, where eluent A: 0.1% HCOOH in water, eluent B: 0.1% HCOOH in acetonitrile.

Supplementary Table 2. Fitted parameters of representative dimers in the foldamer system

Compounds	s(r) $\times 10^2 cm^4 mW^{-2}M^{-1}s^{-1}$	r $\times 10^{10}cm^4mW^{-2}M^{-2}s^{-1}$	b $\times 10^{-2}cm\,mW^{-1/2}s^{-1}$	RMSD $10^{-10}\,M\,s^{-1}$
KW-TW	32.71	17.59	2.69	3.33
QW-SW	23.40	9.10	1.50	2.58
RF-QW	22.19	6.63	1.08	4.17
RW-IF	1.72	13.47	2.16	0.60
RW-LW	2.08	3.54	0.61	0.75
RW-QW	24.66	6.83	1.12	3.08
WF-IF	12.86	13.49	2.26	1.76
WF-LW	39.87	13.18	2.21	3.70
WF-RW	17.91	12.49	2.15	2.88
WF-VW	10.30	18.17	3.03	1.12
WF-YF	15.92	28.77	4.58	1.88
WW-IF	20.56	24.32	3.73	3.39
WW-RF	9.04	7.62	1.32	2.52
YF-IF	7.65	9.67	1.53	1.97
YF-LW	9.84	23.82	3.83	1.19
YF-RF	5.09	7.05	1.13	1.06
YF-RW	6.69	11.98	1.98	1.12
YF-VW	5.80	15.59	2.58	0.84

s(r): rate constant of the formation of dimers via direct radical recombination
r: rate constant of dimer replication
b: rate constant of the breakdown of the dimers

Supplementary Table 3. Fitted parameters of representative dimers in the protein-templated sample

compounds	s(r) $x10^2 cm^4 m\,W^{-2}M^{-1}s^{-1}$	s(PX) $x10^{11}cm^4 m\,W^{-2}M^{-2}s^{-1}$	r $x10^{10}cm^4 m\,W^{-2}M^{-2}s^{-1}$	b $x\,10^{-2}cm\,mW^{-1/2}s^{-1}$	P_{tot} (nM)	$K_{d,PX}$ (nM)	K_{XX} (uM)	RMSD $10^{-9}\,M\,s^{-1}$
KW-TW	50.35	3.06	19.47	3.54	149.88	10.30	1.98	1.59
QW-SW	65.67	1.75	1.88	2.23	416.50	483.00	2.13	1.39
RF-QW	60.58	1.06	3.03	1.61	755.40	568.20	0.95	0.50

RW-IF	93.19	2.11	5.76	2.96	409.41	1.90	2.00	0.43
RW-LW	14.82	3.88	10.55	4.04	229.40	0.21	1.70	1.06
RW-QW	39.28	3.68	8.21	3.47	186.57	31.38	1.50	1.09
WF-IF	10.02	3.32	12.53	3.62	106.21	2.48	1.50	0.27
WF-LW	36.05	5.01	23.81	5.69	212.32	1.20	2.00	0.57
WF-RW	113.56	0.91	2.47	1.45	512.33	0.74	2.30	0.99
WF-VW	7.44	3.55	12.50	3.83	79.86	1.24	1.20	0.29
WF-YF	9.33	5.91	29.46	6.43	75.23	1.60	1.00	0.23
WW-IF	21.56	1.93	1.14	1.91	242.39	2.10	1.90	0.79
WW-RF	47.33	1.87	9.79	2.24	277.50	0.78	2.23	0.99
YF-IF	19.74	5.08	15.16	2.43	11.96	0.40	1.00	0.70
YF-LW	11.80	6.28	34.38	6.87	104.00	5.20	1.40	0.49
YF-RF	38.59	4.28	17.95	4.27	176.91	7.76	1.75	0.38
YF-RW	21.06	3.40	14.26	4.04	203.92	1.75	1.55	0.41
YF-VW	4.78	5.14	21.03	4.91	68.40	11.78	1.05	0.34

s(r): rate constant of the formation of dimers via direct radical recombination

s(PX): rate constant of protein-dependent autocatalytic replication

r: rate constant of dimer replication

b: rate constant of the breakdown of the dimers

Pt: total protein concentration

$K_{d,PX}$: dissociation constant of the protein-dimer complex

K_{XX}: dissociation constant of the foldamer self-associate

Supplementary Table 4. Amplification factors of the building blocks in equilibrium and in steady-state.

Equilibrium					Dissipative selection			
#	Name	mean AF	SD		#	Name	mean AF	SD
1	**WF-RW**	9.87	1.66		1	**WW-RF**	23.64	5.41
2	**LW-RW**	7.79	2.43		2	**WF-RW**	22.46	5.22
3	**WF-KW**	7.62	1.35		3	**WF-RF**	15.26	2.65
4	**WW-RW**	7.59	1.22		4	**WF-KW**	14.49	2.08
5	**WW-KW**	7.51	1.32		5	**KW-LW**	12.53	0.95
6	**WF-RF**	7.39	1.03		6	**IF-RF**	10.21	1.33
7	**LW-KW**	6.62	1.27		7	**LW-RW**	9.78	1.03
8	**WW-RF**	6.50	0.82		8	**IF-RW**	8.99	0.77
9	**VW-RW**	5.71	1.29		9	**LW-RF**	8.88	0.77
10	**YF-RW**	5.70	1.42		10	**VW-RW**	7.47	0.72
11	**YF-KW**	5.58	0.96		11	**RF-VW**	7.10	0.72
12	**RF-LW**	5.57	1.25		12	**WF-SW**	6.99	0.36
13	**RW-IF**	5.57	1.25		13	**YF-RW**	6.86	0.88
14	**RF-VW**	5.50	1.30		14	**WF-TW**	5.91	0.68
15	**KW-IF**	5.37	0.68		15	**LW-QW**	5.47	0.91
16	**RF-IF**	4.98	1.05		16	**WF-VW**	5.43	0.40

17	**YF-RF**	4.95	0.67		17	**WF-QW**	5.41	1.38
18	**KW-VW**	4.27	0.99		18	**YF-RF**	5.28	0.61
19	**WW-QW**	4.25	0.31		19	**LW-TW**	4.96	0.73
20	**YF-YF**	4.16	1.02		20	**KW-IF**	4.87	0.70
21	**WF-QW**	4.02	0.45		21	**WW-SW**	4.56	0.63
22	**VW-QW**	3.86	0.60		22	**LW-SW**	4.49	0.30
23	**LW-IF**	3.65	0.42		23	**VW-TW**	4.34	0.49
24	**VW-SW**	3.52	0.66		24	**IF-QW**	4.34	0.50
25	**WF-SW**	3.47	0.08		25	**YF-KW**	4.32	0.51
26	**WF-TW**	3.41	0.14		26	**IF-SW**	4.07	0.57
27	**RW-RF**	3.39	1.38		27	**IF-TW**	4.05	0.36
28	**RW-KW**	3.32	1.32		28	**WF-YF**	3.99	2.38
29	**IF-IF**	3.31	0.57		29	**VW-SW**	3.92	0.39
30	**LW-LW**	3.18	0.84		30	**YF-IF**	3.88	0.37
31	**WW-SW**	3.17	0.38		31	**TW-TW**	3.79	0.74
32	**YF-TW**	3.10	0.39		32	**YF-SW**	3.68	0.68
33	**WW-WW**	2.95	1.06		33	**WF-IF**	3.51	0.52
34	**LW-SW**	2.92	0.14		34	**YF-VW**	3.38	0.60
35	**TW-TW**	2.91	0.05		35	**YF-QW**	3.19	0.89
36	**YF-IF**	2.91	0.31		36	**WF-LW**	3.17	0.56
37	**WF-WW**	2.87	0.52		37	**YF-LW**	3.03	0.52
38	**WF-WF**	2.85	1.16		38	**VW-VW**	2.97	0.77
39	**WF-VW**	2.83	0.45		39	**IF-IF**	2.95	0.43
40	**YF-QW**	2.79	0.42		40	**YF-TW**	2.93	0.24
41	**LW-TW**	2.76	0.15		41	**LW-LW**	2.85	0.59
42	**WW-TW**	2.75	0.21		42	**WF-WW**	2.82	0.53
43	**RW-TW**	2.75	0.96		43	**IF-VW**	2.82	0.52
44	**VW-VW**	2.69	0.10		44	**WF-WF**	2.74	0.61
45	**WW-IF**	2.62	0.55		45	**TW-QW**	2.67	0.53
46	**RF-TW**	2.61	1.34		46	**VW-QW**	2.65	0.24
47	**IF-SW**	2.59	0.41		47	**KW-VW**	2.59	0.58
48	**YF-LW**	2.58	0.12		48	**WW-TW**	2.54	0.79
49	**LW-QW**	2.58	0.20		49	**RW-RW**	2.53	0.42
50	**WW-YF**	2.57	0.63		50	**LW-VW**	2.45	0.36
51	**YF-SW**	2.57	0.35		51	**LW-IF**	2.24	0.42
52	**LW-VW**	2.57	0.36		52	**WW-IF**	2.19	0.57
53	**RW-SW**	2.56	0.84		53	**WW-LW**	2.14	0.36
54	**WF-LW**	2.56	0.70		54	**YF-YF**	2.09	0.09
55	**IF-TW**	2.55	0.47		55	**WW-VW**	1.95	0.29
56	**RW-QW**	2.55	1.29		56	**WW-RW**	1.91	0.69
57	**WF-YF**	2.53	0.22		57	**WW-YF**	1.88	0.91
58	**YF-VW**	2.52	0.06		58	**LW-SG**	1.78	0.46
59	**KW-TW**	2.49	1.26		59	**RF-TW**	1.72	0.34
60	**IF-VW**	2.40	0.04		60	**RW-RF**	1.69	0.06
61	**RF-RF**	2.40	1.46		61	**QW-QW**	1.63	0.09

62	**WW-LW**	2.38	0.49		62	**WW-WW**	1.61	0.10
63	**WF-IF**	2.36	0.28		63	**SW-QW**	1.60	0.15
64	**TW-QW**	2.27	0.40		64	**TW-SW**	1.57	0.11
65	**WW-VW**	2.27	0.20		65	**RW-SW**	1.52	0.10
66	**RF-SW**	2.24	1.11		66	**RF-RF**	1.52	0.10
67	**VW-TW**	2.17	0.22		67	**SW-SW**	1.48	0.14
68	**RF-QW**	2.12	1.04		68	**RW-KW**	1.46	0.03
69	**KW-SW**	2.05	0.90		69	**KW-RF**	1.46	0.06
70	**KW-QW**	2.03	1.04		70	**RF-QW**	1.39	0.08
71	**RF-SG**	2.00	0.67		71	**RW-TW**	1.36	0.06
72	**RW-RW**	1.97	1.58		72	**RW-QW**	1.35	0.47
73	**TW-SG**	1.97	0.62		73	**YF-SG**	1.25	0.05
74	**QW-QW**	1.94	0.31		74	**RF-SW**	1.22	0.40
75	**LW-SG**	1.86	0.40		75	**KW-TW**	1.18	0.20
76	**KW-RF**	1.82	0.49		76	**WW-KW**	1.17	0.06
77	**SW-SG**	1.82	0.51		77	**KW-KW**	1.13	0.10
78	**RW-SG**	1.75	0.55		78	**KW-SW**	1.11	0.09
79	**TW-SW**	1.73	0.31		79	**KW-QW**	1.09	0.09
80	**QW-SG**	1.73	0.43		80	**WW-QW**	1.06	0.33
81	**IF-SG**	1.73	0.76		81	**QW-SG**	1.06	0.05
82	**KW-SG**	1.68	0.47		82	**SW_SG**	1.03	0.06
83	**SW-SW**	1.65	0.00		83	**WW-SG**	1.00	0.04
84	**SW-QW**	1.61	0.37		84	**TW-SG**	0.99	0.19
85	**WF-SG**	1.58	0.84		85	**IF-SG**	0.93	0.18
86	**IF-QW**	1.55	0.56		86	**WF-SG**	0.90	0.38
87	**WW-SG**	1.54	0.80		87	**VW-SG**	0.80	0.16
88	**YF-SG**	1.41	0.62		88	**KW-SG**	0.75	0.06
89	**VW-SG**	1.40	0.59		89	**RF-SG**	0.74	0.04
90	**KW-KW**	1.02	1.09		90	**RW-SG**	0.66	0.05

Supplementary Table 5. Amplification factors of the building blocks in steady state measured with different power densities.

| \multicolumn{4}{c}{Dissip. system (2.55 mW cm^{-2})} | | | | \multicolumn{4}{c}{Dissip. system (3.8 mW cm^{-2})} | | | |

#	Name	mean AF	SD	#	Name	mean AF	SD
1	**RW-KW**	8.79	0.76	1	**WF-RW**	14.07	2.87
2	**VW-QW**	6.99	0.87	2	**WW-RF**	14.07	2.87
3	**WF-QW**	6.79	2.10	3	**WF-KW**	12.83	5.04
4	**RF-TW**	4.78	0.25	4	**RW-LW**	12.30	1.71
5	**YF-YF**	4.64	0.96	5	**KW-LW**	12.16	1.98
6	**KW-SW**	2.80	0.15	6	**WF-RF**	11.60	2.63
7	**RW-LW**	2.66	1.04	7	**RW-VW**	8.10	0.81
8	**RF-QW**	2.57	0.13	8	**LW-QW**	7.35	1.57
9	**RF-SW**	2.55	0.23	9	**WF-SW**	7.27	1.61
10	**YF-KW**	2.26	0.30	10	**RF-IF**	7.05	1.24
11	**WW-RF**	2.24	0.07	11	**YF-RW**	7.00	0.83
12	**RF-LW**	2.09	0.19	12	**RF-VW**	6.96	0.77
13	**RW-SW**	2.08	0.15	13	**WF-TW**	6.88	1.62
14	**WF-SG**	2.07	0.03	14	**RF-LW**	6.56	0.71
15	**TW-QW**	2.06	0.42	15	**RW-IF**	6.56	0.71
16	**KW-QW**	2.00	0.24	16	**YF-KW**	6.49	0.46
17	**RW-TW**	2.00	0.24	17	**WF-QW**	6.47	1.50
18	**WF-RF**	1.98	0.15	18	**LW-SW**	6.06	1.28
19	**KW-IF**	1.89	0.18	19	**YF-TW**	5.93	1.54
20	**TW-TW**	1.89	0.18	20	**LW-TW**	5.93	1.30
21	**RF-VW**	1.74	0.20	21	**YF-RF**	5.59	0.28
22	**TW-SW**	1.71	0.31	22	**WW-SW**	5.51	0.05
23	**WW-KW**	1.70	0.19	23	**YF-SW**	5.27	1.35
24	**WW-TW**	1.67	0.35	24	**VW-TW**	5.06	0.92
25	**YF-TW**	1.66	0.41	25	**KW-IF**	4.95	0.30
26	**KW-LW**	1.46	0.04	26	**TW-TW**	4.95	0.30
27	**SW-SW**	1.44	0.71	27	**VW-SW**	4.94	0.56
28	**IF-SG**	1.43	0.01	28	**WF-VW**	4.71	1.54
29	**YF-RF**	1.42	0.16	29	**IF-SW**	4.63	0.80
30	**VW-SG**	1.33	0.00	30	**KW-VW**	4.48	0.17
31	**LW-SG**	1.30	0.01	31	**IF-TW**	4.45	0.95
32	**YF-SG**	1.30	0.02	32	**YF-QW**	4.44	0.80
33	**WW-RW**	1.29	0.15	33	**IF-QW**	4.23	0.67
34	**RW-IF**	1.26	0.27	34	**VW-QW**	4.23	0.57
35	**YF-RW**	1.20	0.26	35	**WF-YF**	4.20	1.55
36	**WF-LW**	1.20	0.34	36	**VW-VW**	4.19	1.53
37	**WW-IF**	1.20	0.34	37	**WW-WW**	4.09	0.17
38	**KW-VW**	1.14	0.21	38	**WF-IF**	4.08	1.60
39	**KW-TW**	1.14	0.05	39	**YF-YF**	4.05	1.76

40	WW-QW	1.11	0.19
41	RW-RF	1.10	0.13
42	KW-RF	1.08	0.03
43	WW-SW	1.05	0.09
44	YF-SW	1.04	0.07
45	WF-IF	1.01	0.02
46	IF-IF	1.00*	0.00
47	IF-QW	1.00*	0.00
48	IF-SW	1.00*	0.00
49	IF-TW	1.00*	0.00
50	IF-VW	1.00*	0.00
51	LW-IF	1.00*	0.00
52	LW-LW	1.00*	0.00
53	LW-QW	1.00*	0.00
54	LW-SW	1.00*	0.00
55	LW-TW	1.00*	0.00
56	LW-VW	1.00*	0.00
57	QW-QW	1.00*	0.00
58	RW-QW	1.00*	0.00
59	RW-RW	1.00*	0.00
60	RW-VW	1.00*	0.00
61	VW-SW	1.00*	0.00
62	VW-TW	1.00*	0.00
63	VW-VW	1.00*	0.00
64	WF-KW	1.00*	0.00
65	WF-RW	1.00*	0.00
66	WF-SW	1.00*	0.00
67	WF-TW	1.00*	0.00
68	WF-VW	1.00*	0.00
69	WF-WF	1.00*	0.00
70	WF-WW	1.00*	0.00
71	WF-YF	1.00*	0.00
72	WW-LW	1.00*	0.00
73	WW-VW	1.00*	0.00
74	WW-WW	1.00*	0.00
75	WW-YF	1.00*	0.00
76	YF-IF	1.00*	0.00
77	YF-LW	1.00*	0.00
78	YF-QW	1.00*	0.00
79	YF-VW	1.00*	0.00
80	TW-SG	0.98	0.02
81	QW-SG	0.96	0.01
82	SW-SG	0.96	0.01
83	KW-KW	0.96	0.09
84	RW-SG	0.95	0.02

40	WW-IF	4.00	1.30
41	YF-VW	3.97	1.59
42	WF-LW	3.93	1.54
43	WF-WW	3.89	1.05
44	LW-VW	3.89	1.29
45	WF-WF	3.84	1.42
46	WW-TW	3.83	0.04
47	WW-YF	3.81	0.78
48	WW-LW	3.73	1.24
49	WW-RW	3.70	0.62
50	WW-VW	3.66	0.79
51	RW-RW	3.61	0.36
52	YF-IF	3.57	1.46
53	TW-QW	3.43	0.10
54	LW-LW	3.41	1.42
55	YF-LW	3.40	1.32
56	IF-VW	3.38	1.31
57	IF-IF	3.09	1.23
58	LW-IF	2.86	1.05
59	RW-TW	2.70	0.08
60	WW-QW	2.61	0.10
61	TW-SW	2.16	0.09
62	RW-KW	2.14	0.03
63	RW-SW	2.11	0.19
64	WW-KW	2.10	0.06
65	RF-TW	2.05	0.00
66	RW-QW	2.02	0.12
67	KW-TW	1.96	0.15
68	SW-QW	1.88	0.19
69	SW-SW	1.86	0.02
70	QW-QW	1.85	0.15
71	RW-RF	1.74	0.13
72	RF-RF	1.69	0.03
73	WF-SG	1.66	0.05
74	RF-SW	1.58	0.09
75	KW-SW	1.52	0.09
76	KW-RF	1.47	0.11
77	LW-SG	1.45	0.31
78	RF-QW	1.45	0.02
79	KW-KW	1.41	0.07
80	KW-QW	1.39	0.13
81	IF-SG	1.36	0.02
82	YF-SG	1.31	0.00
83	VW-SG	1.23	0.02
84	TW-SG	1.02	0.04

29

85	**RF-SG**	0.95	0.01
86	**RF-RF**	0.94	0.01
87	**KW-SG**	0.93	0.01
88	**WW-SG**	0.88	0.02
89	**SW-QW**	0.75	0.19
90	**RF-IF**	0.37	0.02

85	**WW-SG**	0.99	0.08
86	**SW-SG**	0.97	0.05
87	**QW-SG**	0.93	0.08
88	**RF-SG**	0.92	0.00
89	**KW-SG**	0.90	0.01
90	**RW-SG**	0.89	0.02

*amount of building block was under the detection limit; minimum detectable AUC (5E+05 AU) was used for calculations.

Supplementary Table 6. Amplification factors of the building blocks in steady state as a function of CaM concentration.

1 µM CaM					12 µM CaM			
#	Name	mean AF	SD		#	Name	mean AF	SD
1	**RF-VW**	4.50	0.19		1	**WF-KW**	16.40	0.92
2	**RF-IF**	4.08	1.06		2	**WF-RW**	16.10	1.10
3	**RW-LW**	3.64	1.46		3	**WW-RF**	16.10	1.10
4	**WF-RF**	3.41	1.21		4	**KW-LW**	13.56	0.93
5	**WF-RW**	3.30	0.99		5	**RW-LW**	13.51	0.49
6	**WW-RF**	3.30	0.99		6	**WF-RF**	13.47	0.97
7	**KW-LW**	3.21	1.14		7	**RW-VW**	8.67	0.50
8	**RW-VW**	3.14	0.71		8	**LW-QW**	8.46	0.39
9	**IF-SW**	2.90	0.87		9	**WF-SW**	8.41	0.60
10	**IF-TW**	2.89	0.94		10	**WF-TW**	8.02	0.57
11	**IF-QW**	2.86	0.87		11	**RF-IF**	7.92	0.39
12	**VW-TW**	2.83	0.97		12	**YF-RW**	7.59	0.54
13	**WF-KW**	2.82	0.79		13	**WF-QW**	7.54	0.25
14	**VW-SW**	2.74	1.01		14	**RF-VW**	7.50	0.60
15	**RF-LW**	2.71	0.52		15	**RF-LW**	7.06	0.49
16	**YF-RW**	2.71	0.69		16	**RW-IF**	7.06	0.49
17	**RW-IF**	2.69	0.44		17	**YF-TW**	7.02	0.53
18	**IF-IF**	2.67	0.71		18	**LW-SW**	6.97	0.32
19	**YF-RF**	2.66	0.33		19	**LW-TW**	6.85	0.35
20	**VW-VW**	2.65	0.72		20	**YF-KW**	6.81	0.59
21	**LW-QW**	2.60	0.79		21	**YF-SW**	6.23	0.48
22	**LW-SW**	2.58	0.84		22	**WF-VW**	5.80	0.34
23	**YF-TW**	2.57	0.70		23	**YF-RF**	5.79	0.52
24	**IF-VW**	2.54	0.76		24	**VW-TW**	5.70	0.31
25	**VW-QW**	2.53	0.47		25	**WW-SW**	5.54	0.30
26	**LW-TW**	2.53	0.88		26	**VW-SW**	5.33	0.30
27	**YF-QW**	2.51	0.71		27	**WF-YF**	5.30	0.29
28	**YF-IF**	2.50	0.68		28	**YF-YF**	5.29	0.33
29	**WF-SW**	2.48	0.91		29	**VW-VW**	5.27	0.28

30	WF-QW	2.47	0.80		30	WF-IF	5.21	0.24
31	YF-YF	2.44	0.64		31	IF-SW	5.19	0.31
32	YF-VW	2.42	0.71		32	KW-IF	5.17	0.16
33	WW-LW	2.34	0.75		33	TW-TW	5.17	0.16
34	YF-KW	2.32	0.39		34	IF-TW	5.12	0.42
35	LW-IF	2.32	0.56		35	YF-VW	5.09	0.32
36	LW-VW	2.31	0.52		36	WF-LW	5.02	0.25
37	YF-SW	2.31	0.29		37	YF-QW	5.00	0.10
38	YF-LW	2.30	0.56		38	WW-IF	4.92	0.23
39	LW-LW	2.26	0.50		39	WF-WF	4.85	0.19
40	WF-TW	2.24	0.66		40	LW-VW	4.80	0.32
41	WF-IF	2.21	0.48		41	IF-QW	4.70	0.20
42	WF-VW	2.20	0.47		42	WF-WW	4.63	0.30
43	TW-TW	2.13	0.53		43	VW-QW	4.63	0.09
44	WF-WW	2.13	0.61		44	WW-LW	4.61	0.21
45	WF-YF	2.12	0.47		45	YF-IF	4.61	0.21
46	WW-IF	2.09	0.37		46	LW-LW	4.42	0.20
47	WF-WF	2.09	0.45		47	WW-YF	4.36	0.44
48	KW-IF	2.08	0.51		48	KW-VW	4.36	0.37
49	WF-LW	2.07	0.42		49	YF-LW	4.33	0.24
50	KW-VW	1.97	0.21		50	IF-VW	4.30	0.22
51	WW-YF	1.83	0.55		51	WW-VW	4.22	0.39
52	WW-VW	1.82	0.49		52	WW-WW	3.97	1.97
53	RW-RF	1.65	0.32		53	IF-IF	3.95	0.21
54	QW-QW	1.65	0.26		54	WW-TW	3.86	0.28
55	RW-RW	1.55	0.43		55	LW-IF	3.60	0.22
56	TW-SW	1.53	0.33		56	TW-QW	3.36	0.13
57	SW-QW	1.53	0.31		57	RW-RW	3.36	0.07
58	RF-QW	1.51	0.26		58	WW-RW	3.26	0.07
59	RF-TW	1.50	0.24		59	RW-TW	2.76	0.08
60	WW-SW	1.50	0.15		60	WW-QW	2.54	0.28
61	RW-QW	1.50	0.29		61	WW-KW	2.15	0.11
62	WW-WW	1.48	0.45		62	RW-KW	2.12	0.06
63	TW-QW	1.47	0.25		63	TW-SW	2.09	0.10
64	SW-SW	1.44	0.23		64	RF-TW	2.05	0.06
65	RF-SW	1.43	0.13		65	RW-SW	1.97	0.03
66	KW-RF	1.42	0.26		66	RW-QW	1.93	0.02
67	RW-SW	1.40	0.33		67	SW-SW	1.88	0.02
68	RW-KW	1.34	0.30		68	KW-TW	1.85	0.02
69	KW-TW	1.33	0.16		69	QW-QW	1.75	0.03
70	KW-KW	1.32	0.18		70	SW-QW	1.74	0.02
71	KW-SW	1.32	0.18		71	RF-RF	1.72	0.08
72	KW-QW	1.29	0.20		72	RW-RF	1.65	0.03

73	**RW-TW**	1.28	0.32		73	**RF-SW**	1.64	0.01
74	**WW-RW**	1.25	0.44		74	**WF-SG**	1.63	0.07
75	**WW-TW**	1.21	0.39		75	**LW-SG**	1.47	0.10
76	**RF-RF**	1.17	0.04		76	**KW-SW**	1.45	0.01
77	**WW-QW**	1.12	0.30		77	**RF-QW**	1.44	0.04
78	**WW-KW**	1.09	0.43		78	**KW-RF**	1.40	0.12
79	**SW-SG**	0.93	0.05		79	**KW-KW**	1.37	0.19
80	**LW-SG**	0.93	0.05		80	**IF-SG**	1.34	0.02
81	**RF-SG**	0.92	0.04		81	**YF-SG**	1.32	0.00
82	**KW-SG**	0.90	0.00		82	**KW-QW**	1.30	0.05
83	**IF-SG**	0.90	0.02		83	**VW-SG**	1.24	0.06
84	**YF-SG**	0.89	0.07		84	**SW-SG**	1.01	0.01
85	**QW-SG**	0.89	0.06		85	**TW-SG**	0.99	0.06
86	**RW-SG**	0.88	0.04		86	**QW-SG**	0.99	0.01
87	**TW-SG**	0.85	0.03		87	**WW-SG**	0.94	0.04
88	**WF-SG**	0.85	0.05		88	**RF-SG**	0.92	0.06
89	**VW-SG**	0.83	0.04		89	**KW-SG**	0.89	0.00
90	**WW-SG**	0.75	0.08		90	**RW-SG**	0.88	0.04

Supplementary Table 7. Identification of the oxidised Met residues in the sequence.

m/z monoisotopic	m/z average	Type of modification	Start	End	Sequence	Relative %
805.4236	805.9773		41	47	(K)ELGTVMR(S)	98.1
821.4186	**821.9766**	1Oxidation	41	47	(K)ELGTVMR(S)	1.9
907.4367	907.9584		32	40	(K)DGDGTITTK(E)	
956.4724	957.0774		24	31	(K)EAFSLFDK(D)	
1011.526	1012.16		97	104	(R)EAFRVFDK(D)	
1028.519	1029.21		117	125	(R)HVMTNLGEK(L)	95.2
1044.514	**1045.21**	1Oxidation	117	125	(R)HVMTNLGEK(L)	4.8
1093.464	1094.083		88	96	(K)DTDSEEEIR(E)	
1265.612	1266.361		105	116	(K)DGNGYISAAELR(H)	
1349.625	1350.496		126	136	(K)LTDEEVDEMIR(E)	98.6
1352.6	1353.456		86	96	(K)MKDTDSEEEIR(E)	97.9
1365.62	**1366.496**	1Oxidation	126	136	(K)LTDEEVDEMIR(E)	1.4
1368.595	**1369.456**	1Oxidation	86	96	(K)MKDTDSEEEIR(E)	2.1
1596.714	1597.645		88	100	(K)DTDSEEEIREAFR(V)	
1693.843	1694.913		32	47	(K)DGDGTITTKELGTVMR(S)	
1709.837	**1710.912**	1Oxidation	32	47	(K)DGDGTITTKELGTVMR(S)	NF
1754.871	1755.937		101	116	(R)VFDKDGNGYISAAELR(H)	
1844.891	1846.013		24	40	(K)EAFSLFDKDGDGTITTK(E)	
1940.891	1942.122		7	23	(R)SNSMADQLTEEQIAEFK(E)	98.6
1956.886	**1958.121**	1Oxidation	7	23	(R)SNSMADQLTEEQIAEFK(E)	1.4
2275.114	2276.549		105	125	(K)DGNGYISAAELRHVMTNLGEK(L)	
2291.109	**2292.548**	1Oxidation	105	125	(K)DGNGYISAAELRHVMTNLGEK(L)	NF

2359.127	2360.684		117	136	(R)HVMTNLGEKLTDEEVDEMIR(E)	96
2375.122	**2376.683**	1Oxidation	117	136	(R)HVMTNLGEKLTDEEVDEMIR(E)	4.0
2391.117	**2392.683**	2Oxidation	117	136	(R)HVMTNLGEKLTDEEVDEMIR(E)	NF
2490.08	2491.728		137	158	(R)EADIDGDGQVNYEEFVQMMTAK(-)	
2506.075	**2507.728**	1Oxidation	137	158	(R)EADIDGDGQVNYEEFVQMMTAK(-)	NF
2522.07	**2523.727**	2Oxidation	137	158	(R)EADIDGDGQVNYEEFVQMMTAK(-)	NF
2580.182	2581.86		1	23	(-)GSHMARSNSMADQLTEEQIAEFK(E)	
2596.177	**2597.86**	1Oxidation	1	23	(-)GSHMARSNSMADQLTEEQIAEFK(E)	NF
2612.172	**2613.859**	2Oxidation	1	23	(-)GSHMARSNSMADQLTEEQIAEFK(E)	NF
2622.192	2623.898	1Acetyl	1	23	(-)GSHMARSNSMADQLTEEQIAEFK(E)	NF
2638.187	**2639.897**	1Acetyl 1Oxidation	1	23	(-)GSHMARSNSMADQLTEEQIAEFK(E)	NF
2654.182	**2655.897**	1Acetyl 2Oxidation	1	23	(-)GSHMARSNSMADQLTEEQIAEFK(E)	NF
2878.345	2880.176		7	31	(R)SNSMADQLTEEQIAEFKEAFSLFDK(D)	
2894.34	**2896.176**	1Oxidation	7	31	(R)SNSMADQLTEEQIAEFKEAFSLFDK(D)	NF
3820.687	3823.202		126	158	(K)LTDEEVDEMIREADIDGDGQVNYEEFVQMMTAK(-)	
3836.682	**3839.201**	1Oxidation	126	158	(K)LTDEEVDEMIREADIDGDGQVNYEEFVQMMTAK(-)	NF
3852.677	**3855.201**	2Oxidation	126	158	(K)LTDEEVDEMIREADIDGDGQVNYEEFVQMMTAK(-)	NF
3868.672	**3871.2**	3Oxidation	126	158	(K)LTDEEVDEMIREADIDGDGQVNYEEFVQMMTAK(-)	NF

Product ions were searched based on their expected average m/z and relative ratio of the oxidised and intact protein was estimated with the area under the curve (AUC) of the appropriate fragment using the following formula: Relative % = $AUC_{modified}/(AUC_{modified}+AUC_{intact})$ x 100. Product ions labelled with NF (not found) were not detectable during the measurement.

Supplementary Table 8. Characterisation of the precursor foldameric building blocks

Compounds	Exact mass (Da)	Detected ions		Retention time (min)*	Retention time (min)**
		$[M+1H^+]^{1+}$	$[M+2H^+]^{2+}$		
IF-SG	1327.62	1328.67	664.84	20.81	14.49
KW-SG	1381.69	1382.69	691.85	16.58	10.42
LW-SG	1366.68	1367.68	684.35	21.79	14.76
QW-SG	1381.65	1382.65	691.83	17.48	11.60
RF-SG	1370.68	1371.69	686.35	16.62	10.31
RW-SG	1409.69	1410.7	705.85	18.03	10.56
SW-SG	1340.63	1341.63	671.32	17.23	11.60
TW-SG	1354.64	1355.65	678.33	19.15	12.06
VW-SG	1352.66	1353.67	677.34	20.11	14.05
WF-SG	1400.66	1401.67	701.34	21.37	14.29
WW-SG	1439.67	1440.68	720.84	17.23	12.86
YF-SG	1377.66	1378.65	689.83	18.94	12.98

*Analytical HPLC-UV measurement. Column: Phenomenex Luna C18 (250 x 4.6 mm) Method: 5-80% B during 25 minutes, flow rate: 1.2 mL min^{-1}, where eluent A: 0.1% TFA in water, eluent B: 0.1% TFA and 80% ACN in water.

**Analytical HPLC-MS measurement. Column: Aeris Widepore XB-C18 (250 x 4.6 mm) Method: 5-80% B during 25 minutes, flow rate: 0.7 mL min^{-1}, where eluent A: 0.1% HCOOH in water, eluent B: 0.1% HCOOH in ACN.

Supplementary Table 9. Calculated Shannon diversity indexes from the amplification probabilities showed on Figure 5.

UV power density (mW/cm-2)	CaM concentration (uM)	Calculated ΔI_{Sh}	SD
2.55	6	-0.1942	0.0253
3.80	6	-0.3869	0.0255
5.10	1	-0.0794	0.0177
5.10	6	-0.4230	0.0338
5.10	12	-0.2392	0.0256

Supplementary Table 10. Calculated AUC of 1μM conversion factors for each library members

compounds	calculated concentration (μM)*	mean AUC	SD	AUC of 1 μM unit
IF-IF	0.2083	6738896	167227	**32346754**
IF-QW	0.4167	14321621	1021416	**34371864**
IF-SG	5	233796364	12121312	**46759273**
IF-SW	0.4167	10250563	267887	**24601332**
IF-TW	0.4167	9781464	99474	**23475495**
IF-VW	0.4167	14658581	333948	**35180567**
KW-IF	0.4167	6984610	192959	**16763051**
KW-KW	0.2083	4688541	196654	**22505032**
KW-LW	0.4167	10931447	352192	**26235452**
KW-QW	0.4167	9592254	191099	**23021391**
KW-RF	0.4167	6041711	280144	**14500094**
KW-SG	5	93498264	8075947	**18699653**
KW-SW	0.4167	10307687	34078	**24738429**
KW-TW	0.4167	11140758	215090	**26737798**
KW-VW	0.4167	11219383	61459	**26926498**
LW-IF	0.4167	13317251	59335	**31961377**
LW-LW	0.2083	5459491	232775	**26205601**
LW-QW	0.4167	7510246	171240	**18024575**
LW-SG	5	71564374	1943793	**14312875**
LW-SW	0.4167	7846422	820359	**18831398**

LW-TW	0.4167	7877221	1158047	**18905315**
LW-VW	0.4167	11755384	350708	**28212900**
QW-QW	0.2083	2505601	113767	**12026904**
QW-SG	5	154788096	3212397	**30957619**
RF-IF	0.4167	9685531	98651	**23245255**
RF-LW	0.4167	9423472	313860	**22616315**
RF-QW	0.4167	5395324	470128	**12948767**
RF-RF	0.2083	2600196	66430	**12480959**
RF-SG	5	76355793	557309	**15271159**
RF-SW	0.4167	8404764	40877	**20171417**
RF-TW	0.4167	6458569	88664	**15500554**
RF-VW	0.4167	9015525	232567	**21637242**
RW-IF	0.4167	9139403	235650	**21934550**
RW-KW	0.4167	7268733	135533	**17444946**
RW-LW	0.4167	9690533	135870	**23257261**
RW-QW	0.4167	8128642	168034	**19508725**
RW-RF	0.4167	4839118	14804	**11613873**
RW-RW	0.2083	2840665	146521	**13635212**
RW-SG	5	81307536	3537250	**16261507**
RW-SW	0.4167	9262117	211359	**22229063**
RW-TW	0.4167	5594796	220034	**13427499**
RW-VW	0.4167	10268484	436026	**24644341**
SW-QW	0.4167	7741284	52795	**18579067**
SW-SG	5	214373675	971923	**42874735**
SW-SW	0.2083	4460048	9425	**21408267**
TW-QW	0.4167	6258758	7940	**15021007**
TW-SG	5	205650252	4735772	**41130050**
TW-SW	0.4167	7866053	65835	**18878512**
TW-TW	0.2083	6984610	192959	**33526183**
VW-QW	0.4167	8395542	149336	**20149285**
VW-SG	5	218439667	209807	**43687933**
VW-SW	0.4167	9549648	30622	**22919137**
VW-TW	0.4167	14321621	1021416	**34371864**
VW-VW	0.2083	6719439	16227	**32253357**
WF-IF	0.4167	16802806	261057	**40326702**
WF-KW	0.4167	12948964	294491	**31077488**
WF-LW	0.4167	14057330	138666	**33737565**
WF-QW	0.4167	9308290	140062	**22339878**
WF-RF	0.4167	9750493	108676	**23401163**
WF-RW	0.4167	5231109	21871	**12554652**
WF-SG	5	229629674	1234010	**45925935**
WF-SW	0.4167	10201405	81613	**24483352**
WF-TW	0.4167	10261229	335150	**24626930**

WF-VW	0.4167	12943413	2777026	**31064167**
WF-WF	0.2083	9182636	141237	**44076722**
WF-WW	0.4167	7037382	357237	**16889704**
WF-YF	0.4167	11977596	184803	**28746208**
WW-IF	0.4167	6697741	203025	**16074566**
WW-KW	0.4167	7218262	137235	**17323816**
WW-LW	0.4167	6808518	206582	**16340430**
WW-QW	0.4167	4956501	97189	**11895592**
WW-RF	0.4167	5597430	97043	**13433822**
WW-RW	0.4167	5744039	55944	**13785683**
WW-SG	5	154424106	809265	**30884821**
WW-SW	0.4167	7736738	259061	**18568158**
WW-TW	0.4167	6666086	237986	**15998593**
WW-VW	0.4167	6666086	237986	**15998593**
WW-WW	0.2083	2408501	253201	**11560822**
WW-YF	0.4167	4863880	87381	**11673302**
YF-IF	0.4167	8352642	1717484	**20046325**
YF-KW	0.4167	8037313	69720	**19289535**
YF-LW	0.4167	9072627	56896	**21774286**
YF-QW	0.4167	6032798	175591	**14478703**
YF-RF	0.4167	6941704	43753	**16660077**
YF-RW	0.4167	7672105	108675	**18413037**
YF-SG	5	177069749	1736459	**35413950**
YF-SW	0.4167	6309200	101256	**15142069**
YF-TW	0.4167	6577118	44472	**15785071**
YF-VW	0.4167	10338711	140452	**24812887**
YF-YF	0.2083	2466209	13733	**11837825**

*Calculated from the statistical product distribution
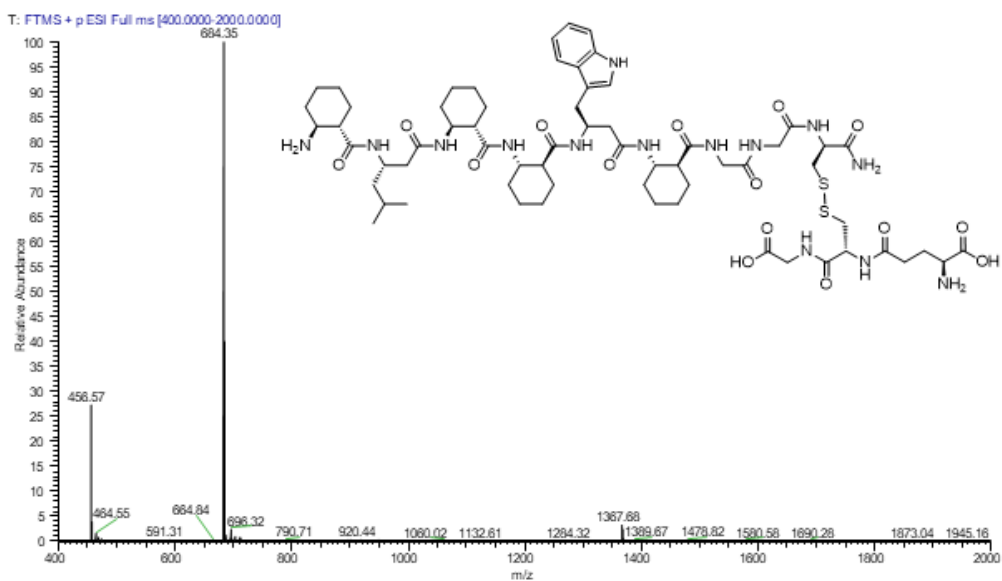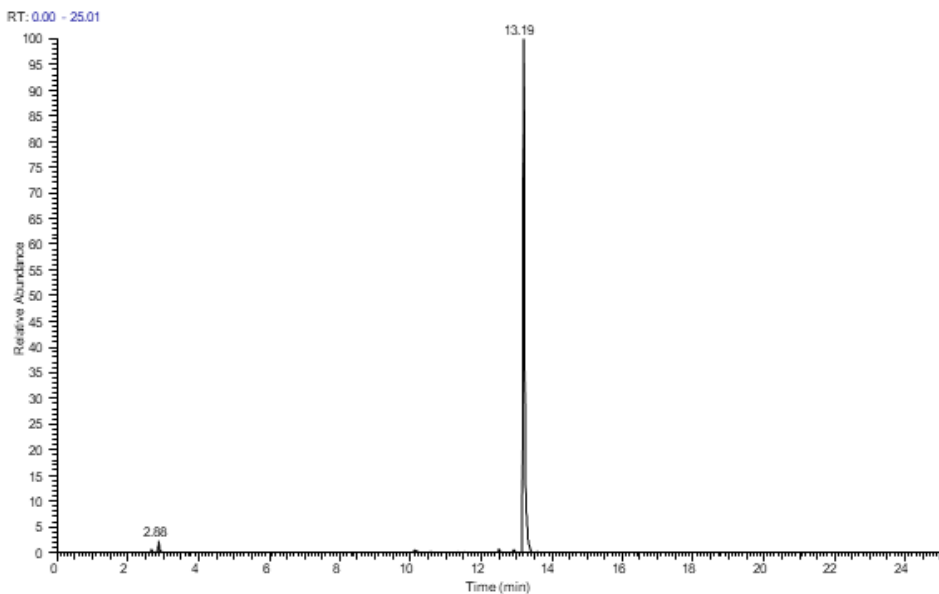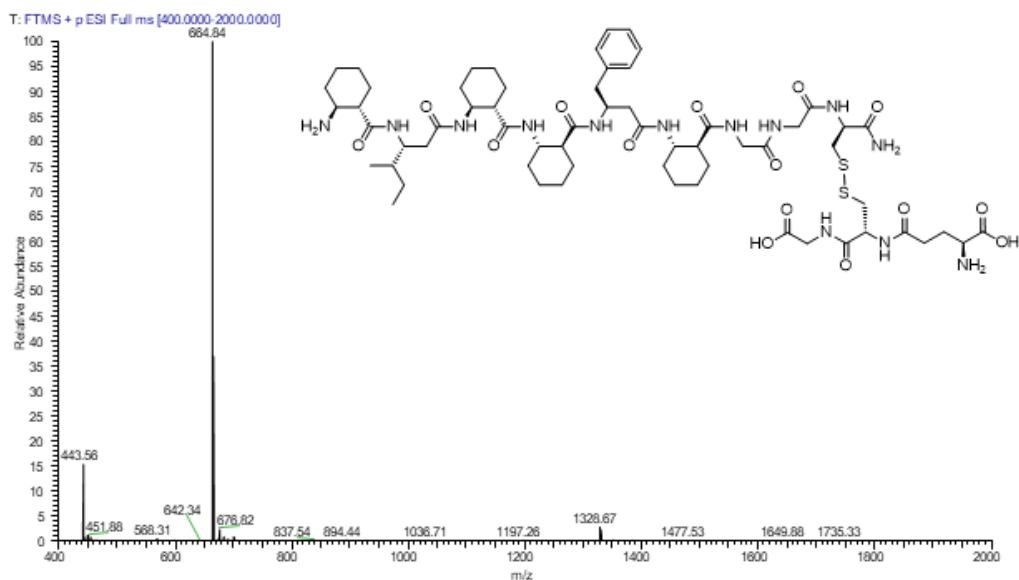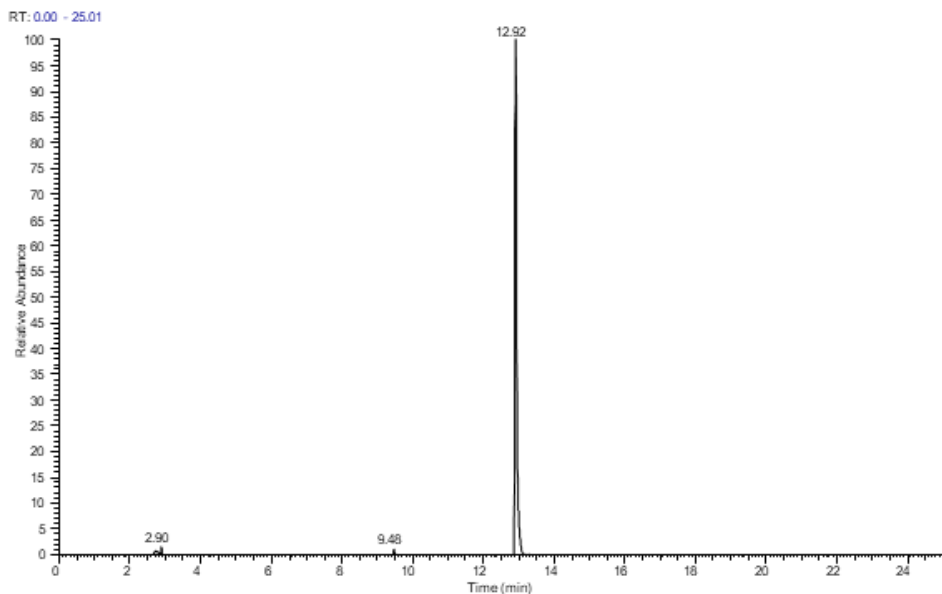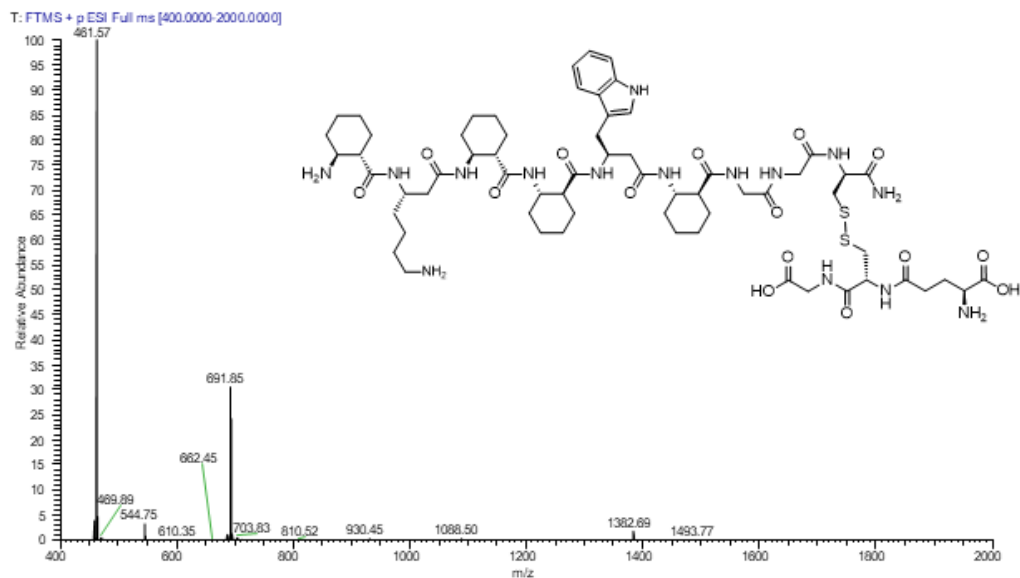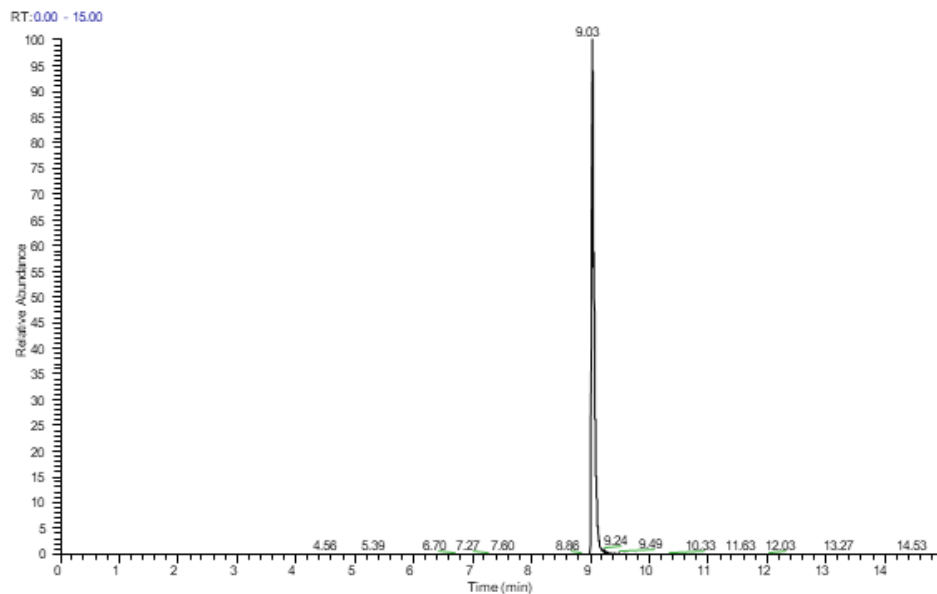
Peptide characterisation data
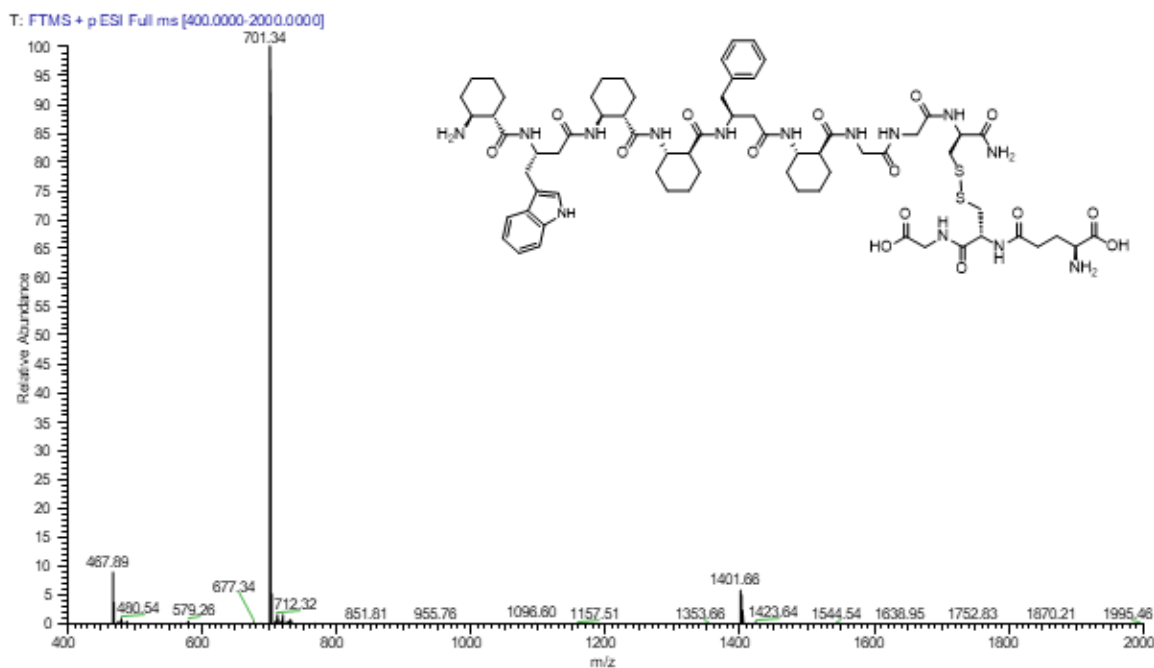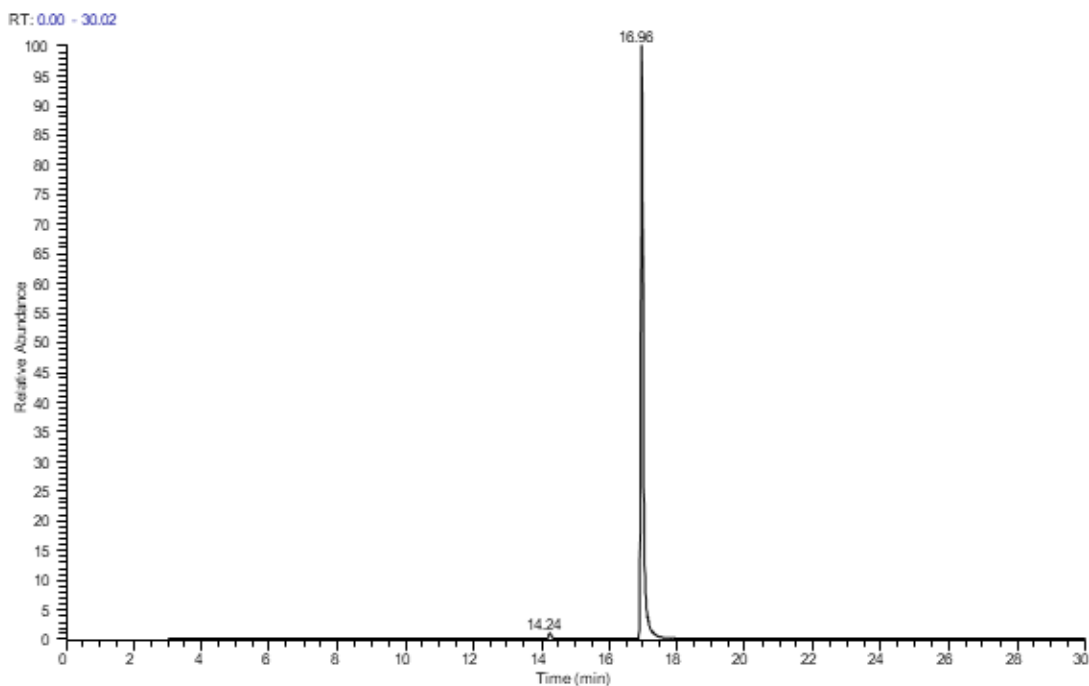
HPLC trace and mass spectrum of the glutathionic precursor **WF-SG** (Exact mass: 1400.66) Calculated isotopic profile for $[M+2H]^{2+}$ (species, abundance): 701.3383 (100%), 701.8400 (72.47%), 702.3417 (25.86%), 702.8379 (6.48%); m/z calculated: 1401.67 $[M+H]^+$, 701.24 $[M+2H]^{2+}$ Observed m/z: 1401.06 $[M+H]^+$, 701.34 $[M+2H]^{2+}$
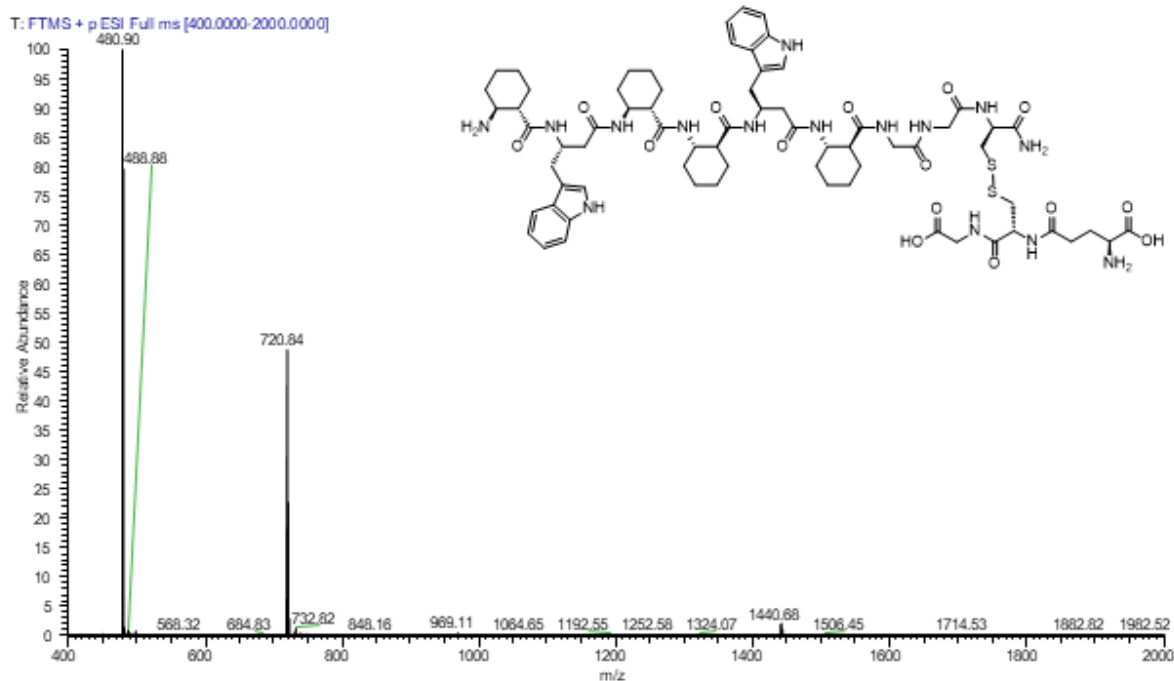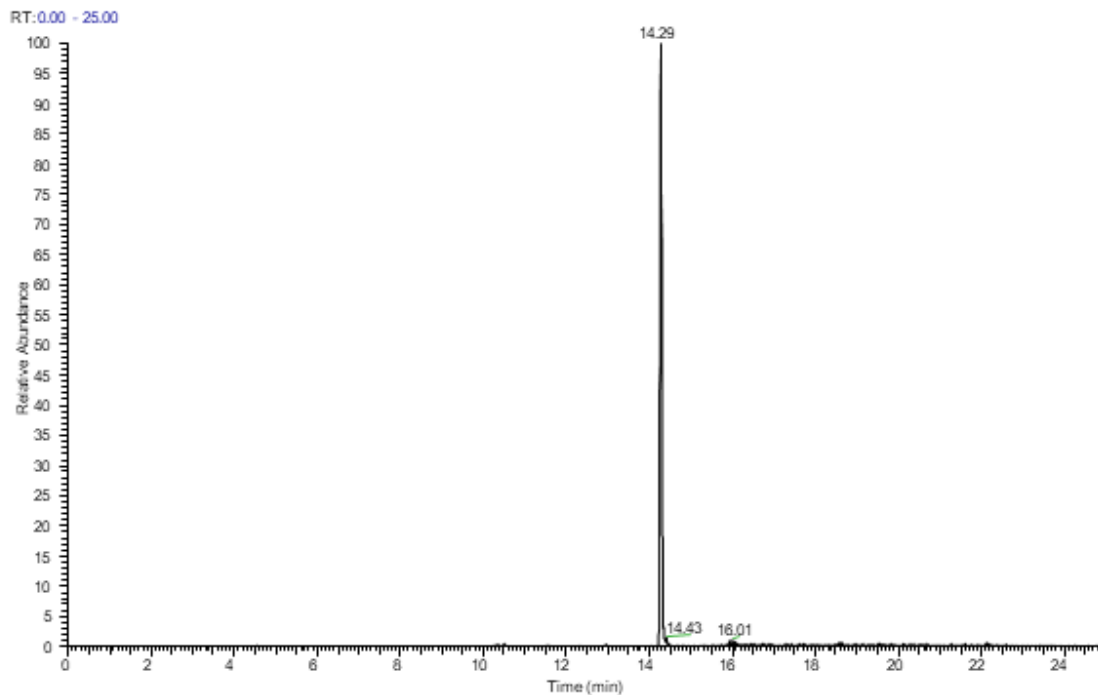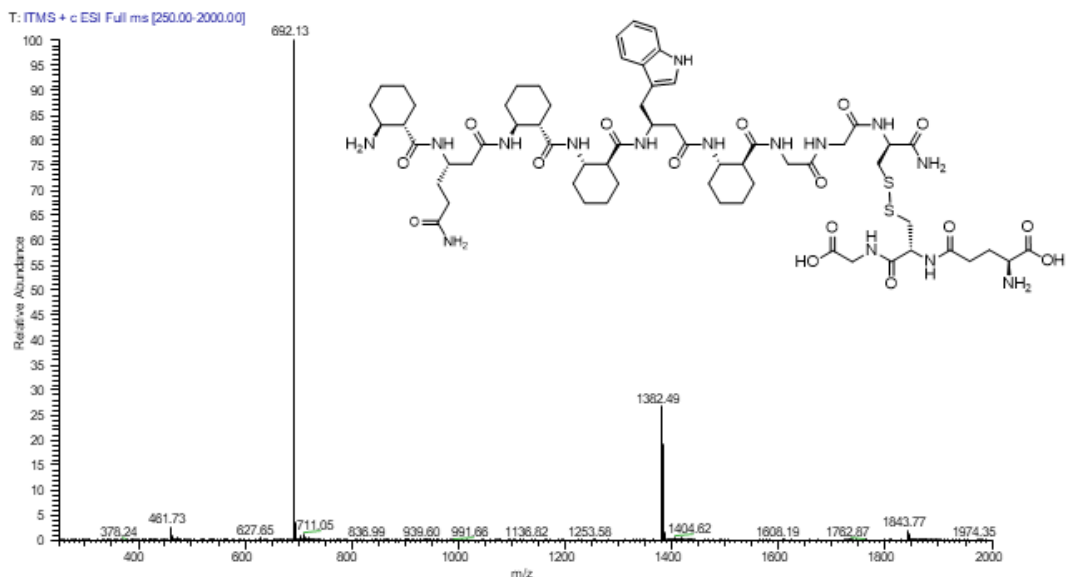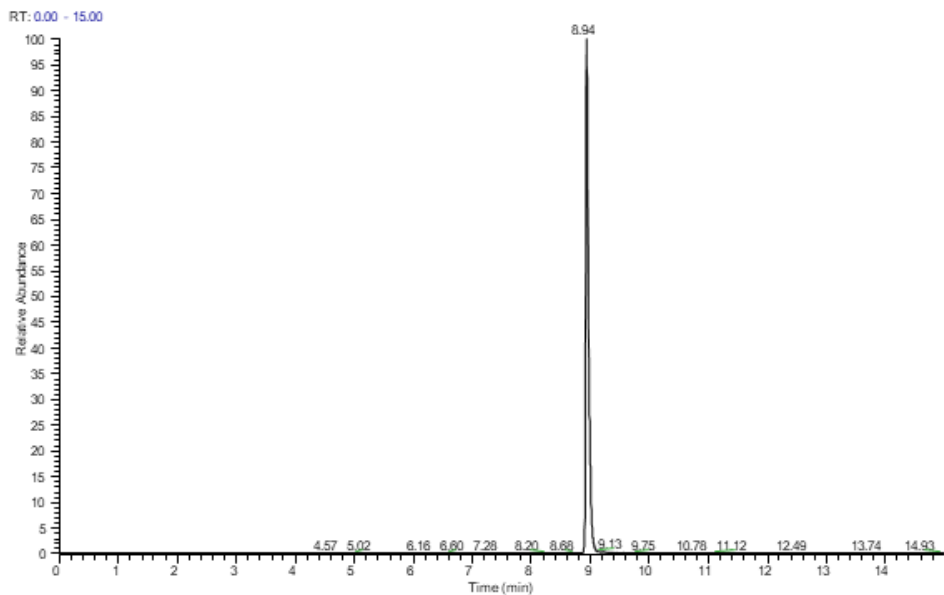
HPLC trace and mass spectrum of the glutathionic precursor **WW-SG** (Exact mass: 1439.67) Calculated isotopic profile for [M+2H]2+ (species, abundance): 720.8438 (100%), 721.3454 (74.63%), 721.8471 (27.44%), 722.3434 (6.78%); m/z calculated: 1440.51 [M+H]$^+$, 720.76 [M+2H]$^{2+}$, 480.84 [M+3H]$^{3+}$; Observed m/z: 1440.68 [M+H]$^+$, 720.64 [M+2H]$^{2+}$, 480.90 [M+3H]$^{3+}$
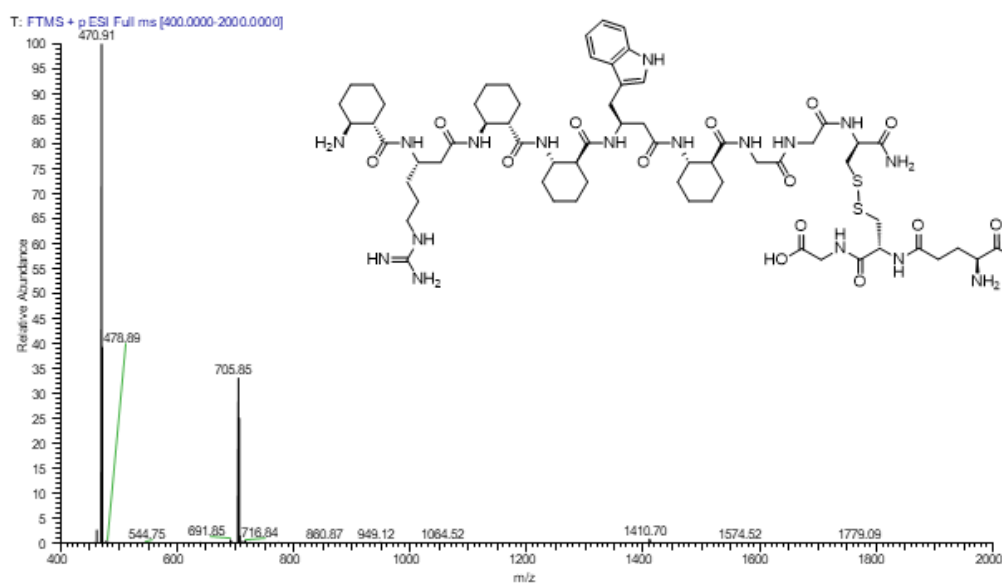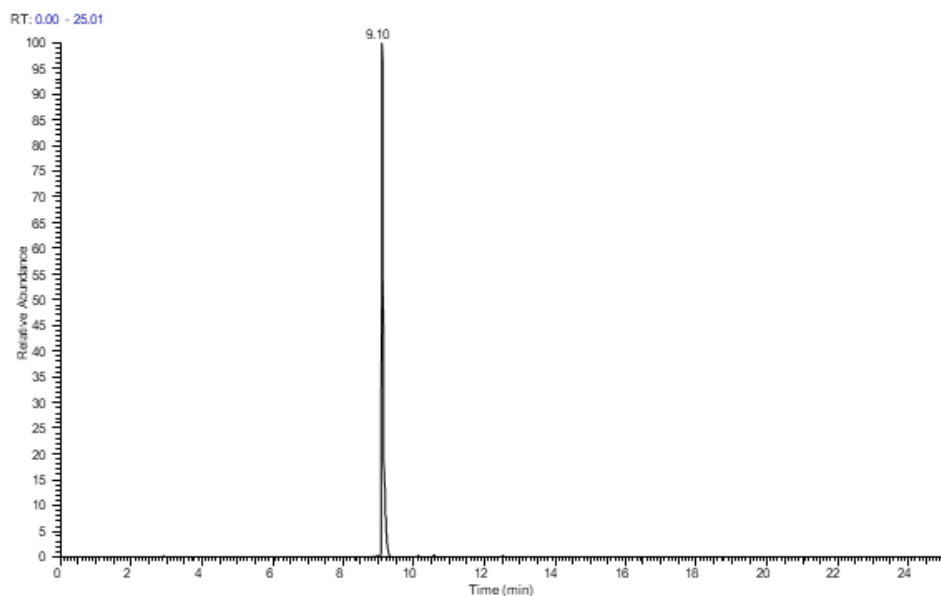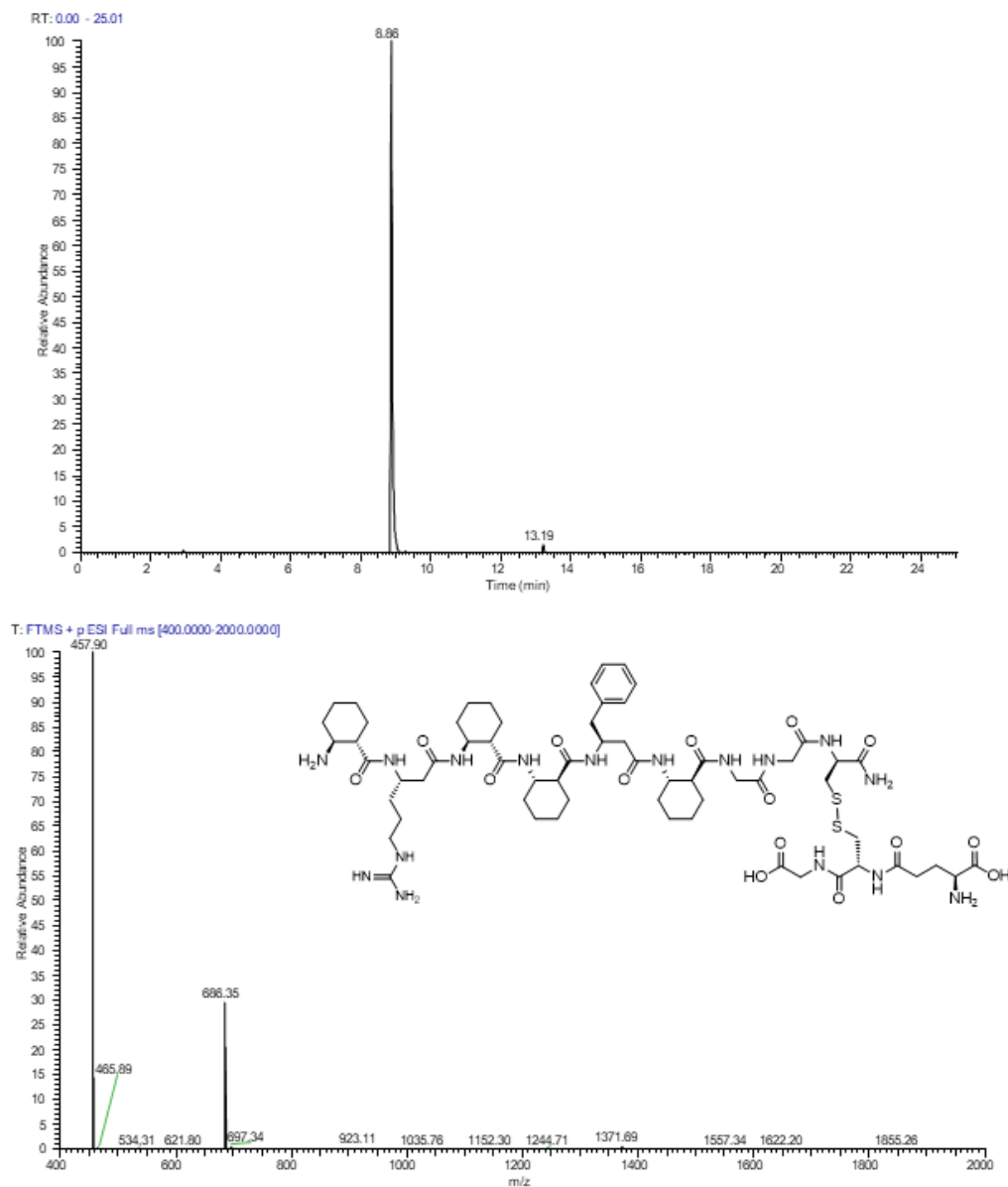
HPLC trace and mass spectrum of the glutathionic precursor **RW-SG** (Exact mass: 1409.69) Calculated isotopic profile for $[M+2H]^{2+}$ (species, abundance): 705.3508 (100%), 705.8524 (69.22%), 706.3487 (8.95%), 706.3510 (4.30%); m/z calculated: 1410.49 $[M+H]^{+}$, 705.75 $[M+2H]^{2+}$, 470.83 $[M+3H]^{3+}$; Observed m/z: 1410.70 $[M+H]^{+}$, 705.85 $[M+2H]^{2+}$, 470.91 $[M+3H]^{3+}$
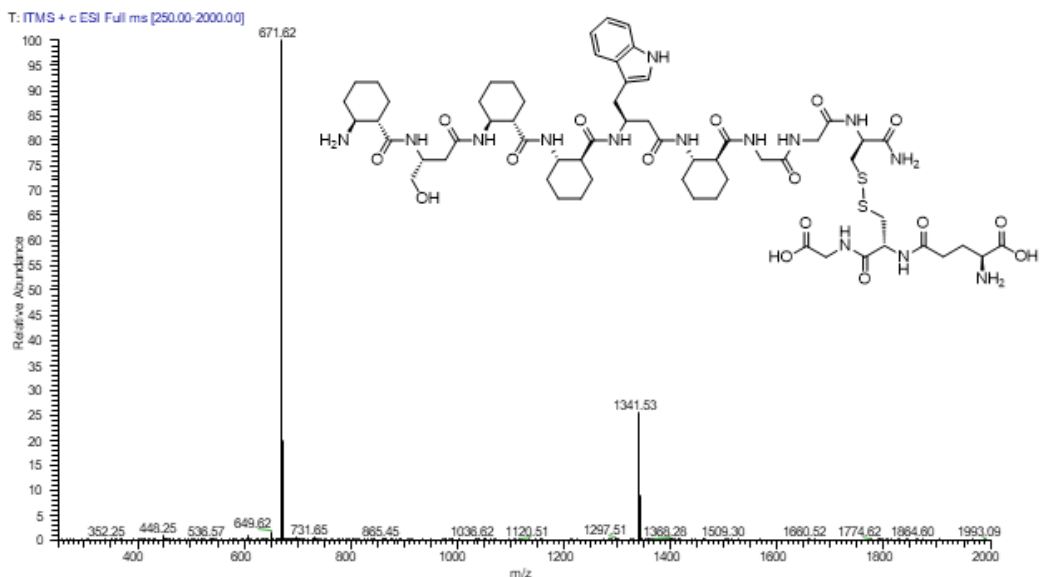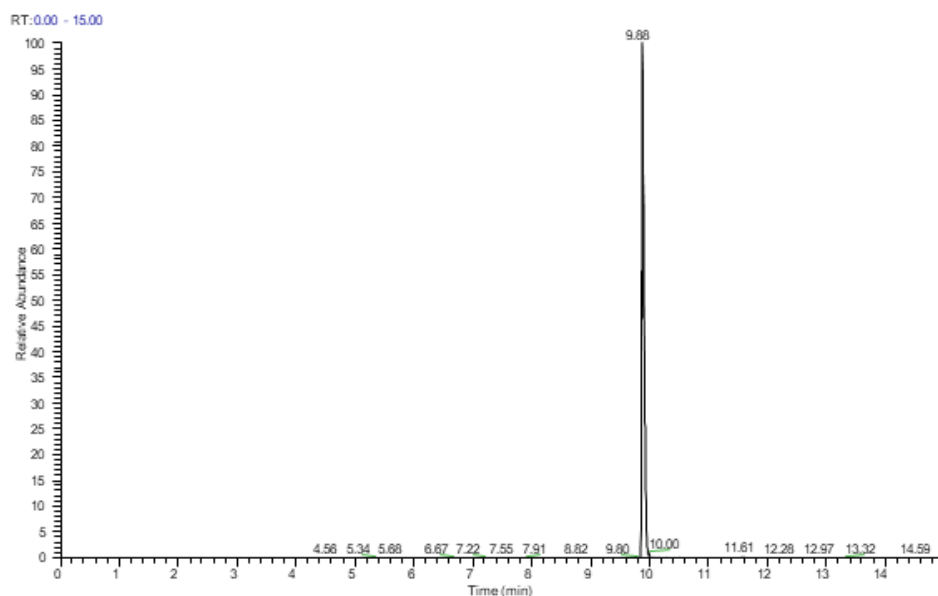
HPLC trace and mass spectrum of the glutathionic precursor **SW-SG** (Exact mass: 1340.63) Calculated isotopic profile for $[M+2H]^{2+}$ (species, abundance): 670.8162 (100%), 671.3179 (65.98%), 671.8141 (8.95%), 671.8164 (3.37%); m/z calculated: 1341.38 $[M+H]^+$, 671.19 $[M+2H]^{2+}$; Observed m/z: 1341.53 $[M+H]^+$, 671.62 $[M+2H]^{2+}$
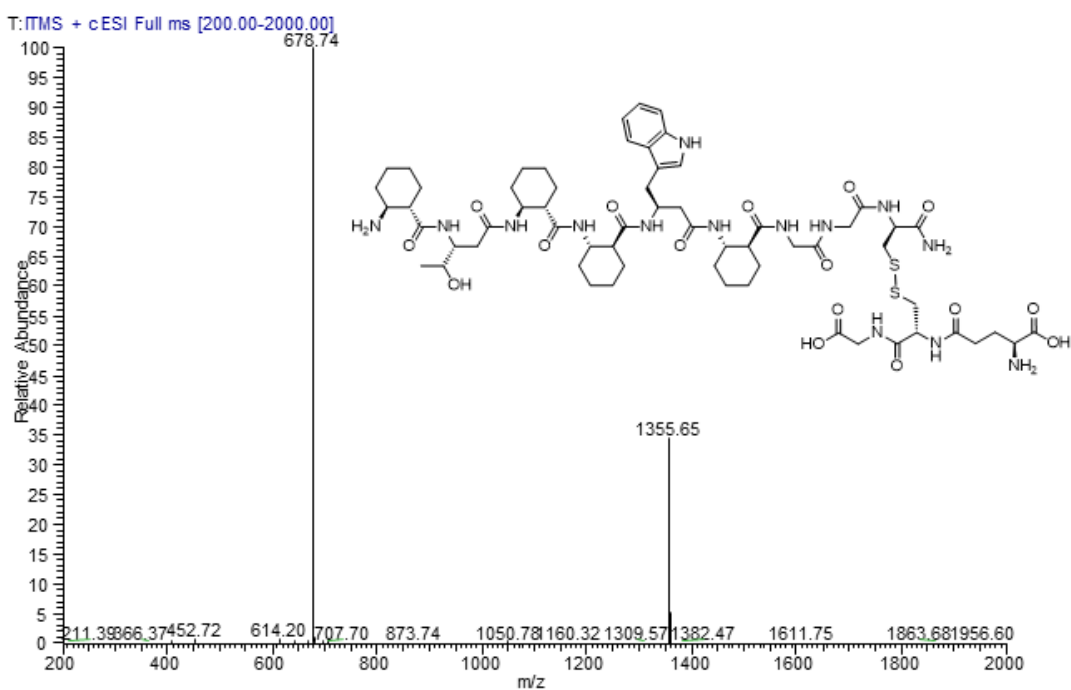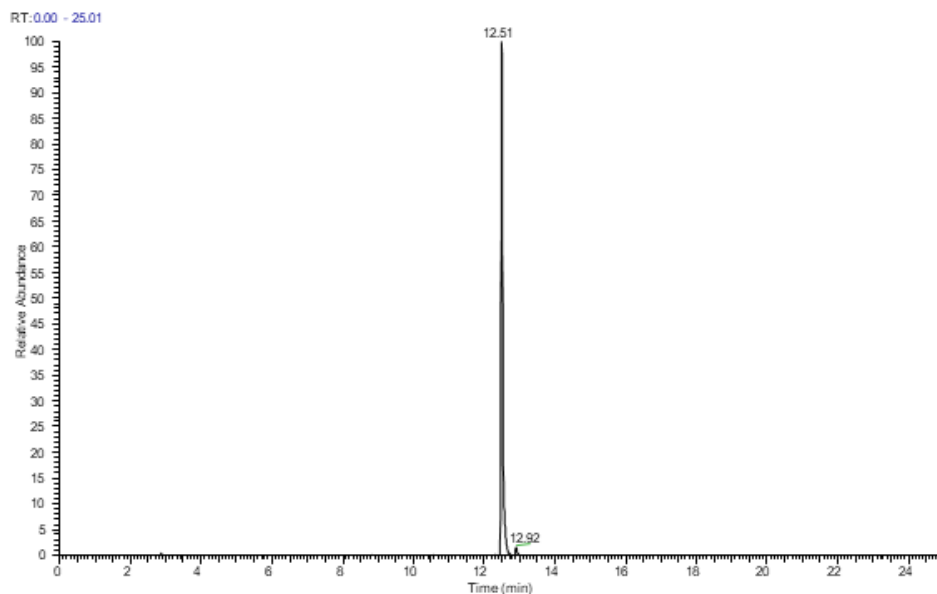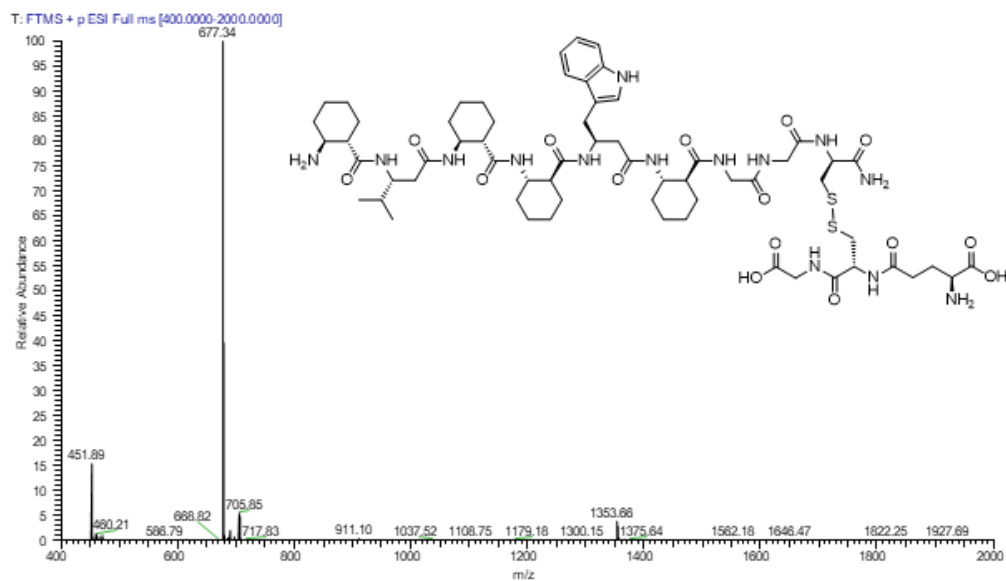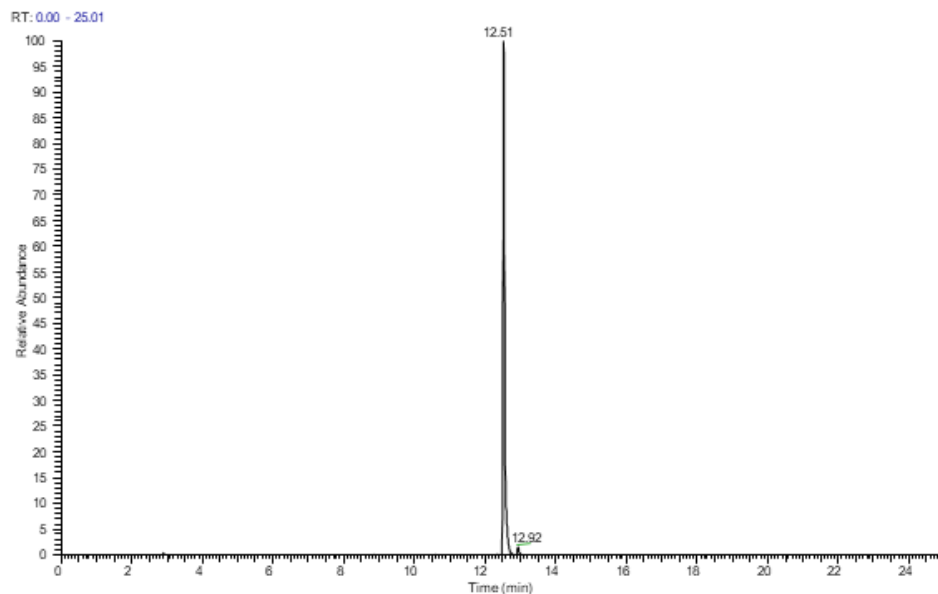
HPLC trace and mass spectrum of the glutathionic precursor **TW-SG** (Exact mass: 1354.64) Calculated isotopic profile for $[M+2H]^{2+}$ (species, abundance): 677.8240 (100%), 678.3257 (67.06%), 678.8211 (8.95%), 678.8242 (3.43%); m/z calculated: 1355.41 $[M+H]^+$, 678.21 $[M+2H]^{2+}$; Observed m/z: 1355.65 $[M+H]^+$, 678.74 $[M+2H]^{2+}$

HPLC trace and mass spectrum of the glutathionic precursor **LW-SG** (Exact mass: 1366.68) Calculated isotopic profile for $[M+2H]^{2+}$ (species, abundance): 683.8422 (100%), 684.3439 (69.22%), 684.8401 (8.95%), 684.8424 (3.54%); m/z calculated: 1367.46 $[M+H]^+$, 684.23 $[M+2H]^{2+}$; Observed m/z: 1367.68 $[M+H]^+$, 684.35 $[M+2H]^{2+}$

HPLC trace and mass spectrum of the glutathionic precursor **IF-SG** (Exact mass: 1327.67) Calculated isotopic profile for $[M+2H]^{2+}$ (species, abundance): 664.3468 (100%), 664.8385 (67.06%), 665.3347 (8.95%), 665.3370 (3.18%); m/z calculated: 1328.42 $[M+H]^+$, 664.71 $[M+2H]^{2+}$; Observed m/z: 1328.67 $[M+H]^+$, 664.84 $[M+2H]^{2+}$
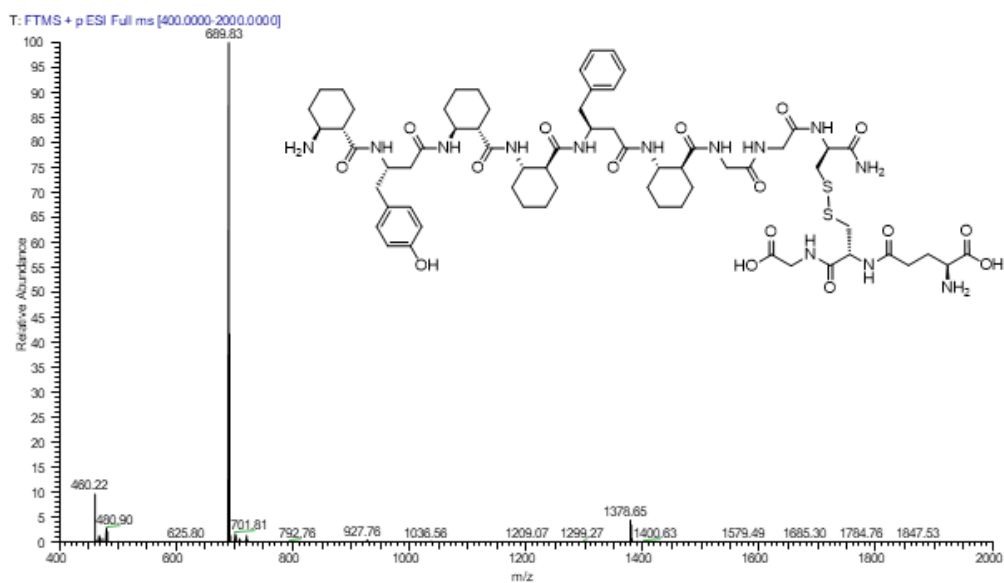
HPLC trace and mass spectrum of the glutathionic precursor **KW-SG** (Exact mass: 1381.69) Calculated isotopic profile for $[M+2H]^{2+}$ (species, abundance): 691.3477 (100%), 691.8494 (69.22%), 692.3447 (8.95%), 692.3479 (3.79%); m/z calculated: 1382.47 $[M+H]^+$, 691.74 $[M+2H]^{2+}$, 461.49 $[M+3H]^{3+}$; Observed m/z: 1382.69 $[M+H]^+$, 691.85 $[M+2H]^{2+}$, 461.57 $[M+3H]^{3+}$

HPLC trace and mass spectrum of the glutathionic precursor **QW-SG** (Exact mass: 1381.65) Calculated isotopic profile for $[M+2H]^{2+}$ (species, abundance): 691.3295 (100%), 691.8312 (68.14%), 692.3274 (8.95%), 692.3297 (3.73%); m/z calculated: 1382.43 $[M+H]^+$, 691.72 $[M+2H]^{2+}$; Observed m/z: 1382.49 $[M+H]^+$, 692.13 $[M+2H]^{2+}$
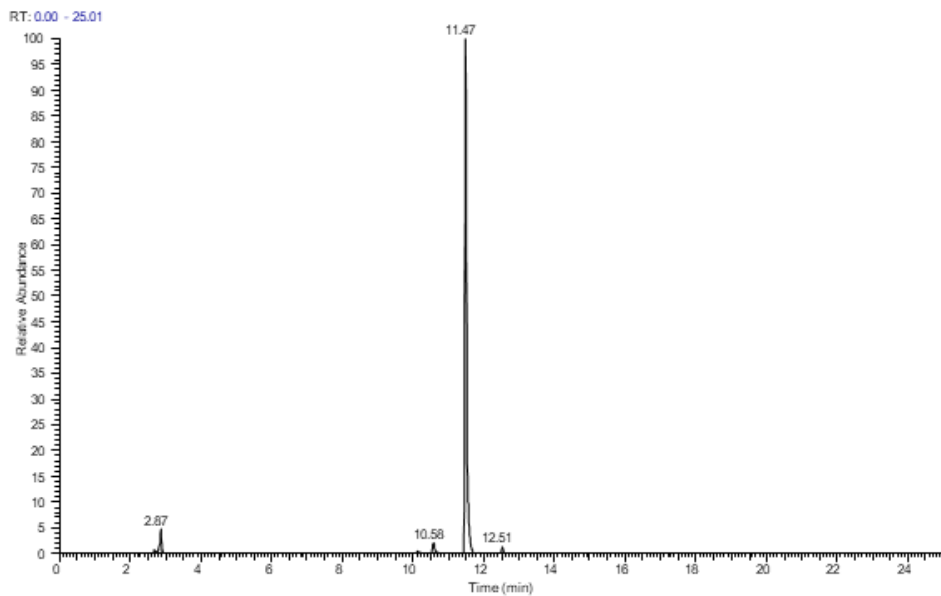
HPLC trace and mass spectrum of the glutathionic precursor **RF-SG** (Exact mass: 1370.68) Calculated isotopic profile for $[M+2H]^{2+}$ (species, abundance): 685.8453 (100%), 686.3470 (67.06%), 686.8432 (8.95%), 686.8455 (3.92%); m/z calculated: 1371.45 $[M+H]^+$, 686.23 $[M+2H]^{2+}$, 457.82 $[M+3H]^{3+}$; Observed m/z: 1371.69 $[M+H]^+$, 686.35 $[M+2H]^{2+}$, 457.90 $[M+3H]^{3+}$
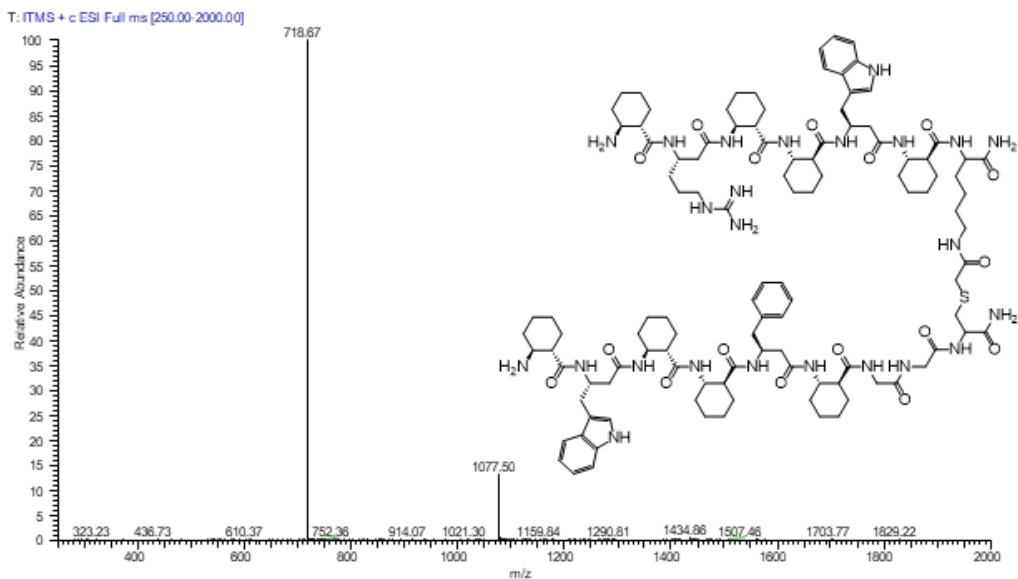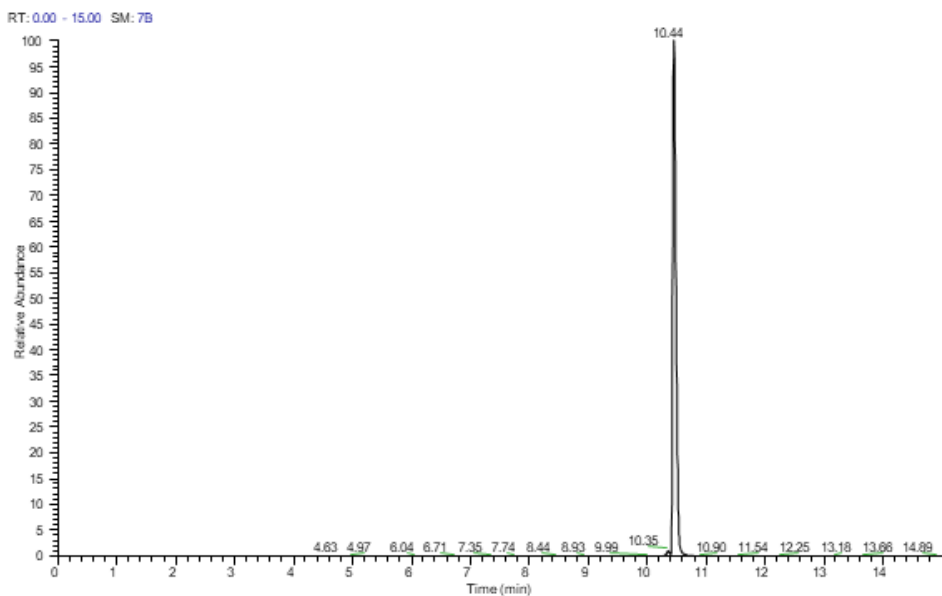
HPLC trace and mass spectrum of the glutathionic precursor **VW-SG** (Exact mass: 1352.66) Calculated isotopic profile for $[M+2H]^{2+}$ (species, abundance): 676.8344 (100%), 677.3361 (68.14%), 677.8323 (8.95%), 677.8346 (3.49%); m/z calculated: 1353.43 $[M+H]^{+}$, 677.22 $[M+2H]^{2+}$; Observed m/z: 1353.66 $[M+H]^{+}$, 677.34 $[M+2H]^{2+}$
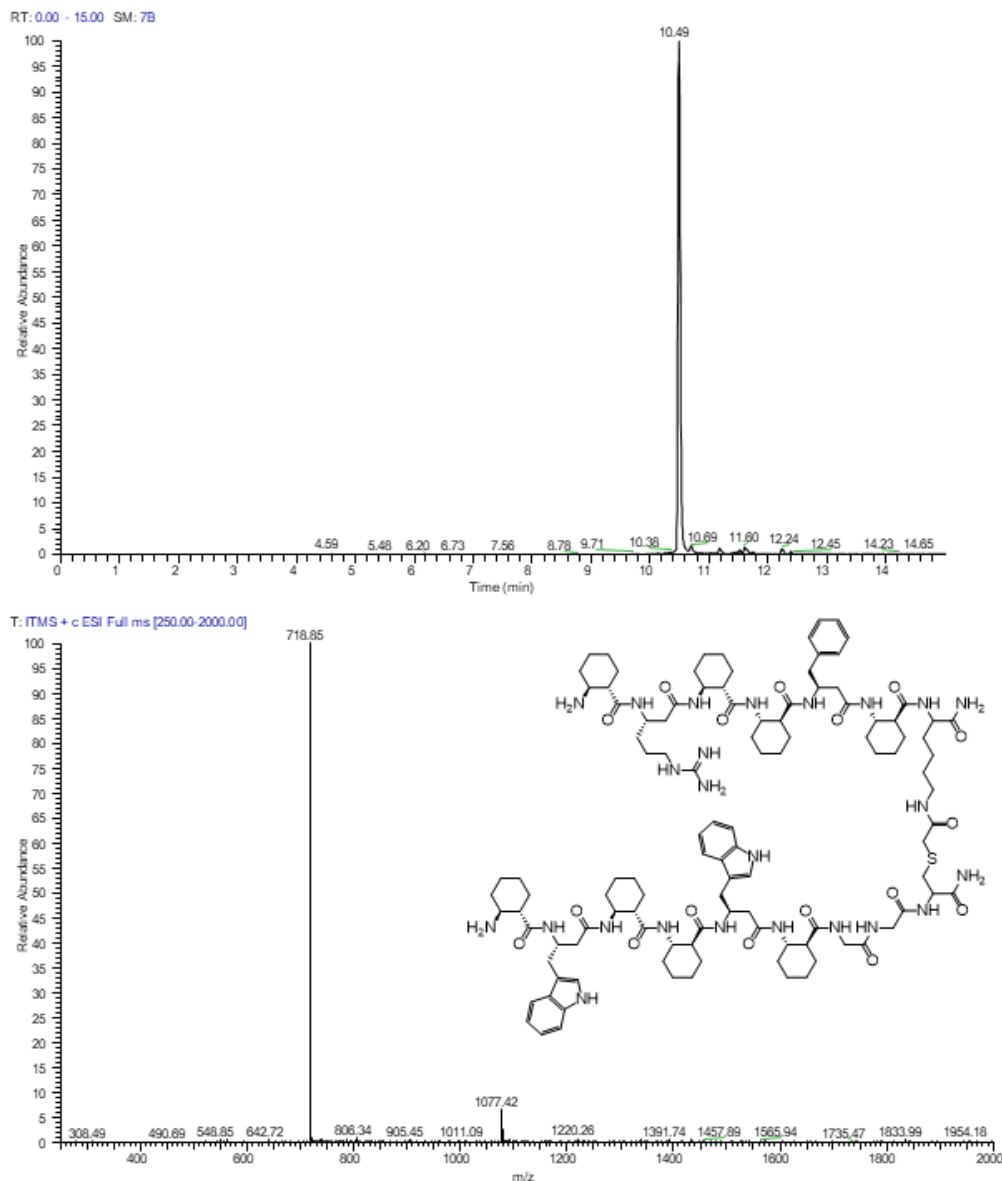
HPLC trace and mass spectrum of the glutathionic precursor **YF-SG** (Exact mass: 1377.65) Calculated isotopic profile for $[M+2H]^{2+}$ (species, abundance): 689.3264 (100%), 689.8281 (70.30%), 690.3243 (8.95%), 690.3266 (3.34%); m/z calculated: 1378.44 $[M+H]^{+}$, 689.72 $[M+2H]^{2+}$; Observed m/z: 1378.65 $[M+H]^{+}$, 689.83 $[M+2H]^{2+}$

HPLC trace and mass spectrum of the glutathionic precursor **WF-S-RW** (Exact mass: 2151.26) Calculated isotopic profile for $[M+3H]^{3+}$ (species, abundance): 717.4215 (80.55%), 717.7560 (100.00%), 718.0883 (8.77%); m/z calculated: 1077.37 $[M+2H]^{2+}$, 718.58 $[M+3H]^{3+}$; Observed m/z: 1077.50 $[M+2H]^{2+}$, 718.67 $[M+3H]^{3+}$

HPLC trace and mass spectrum of the glutathionic precursor **WW-S-RF** (Exact mass: 2151.26) Calculated isotopic profile for $[M+3H]^{3+}$ (species, abundance): 717.4215 (80.55%), 717.7560 (100.00%), 718.0883 (8.77%); m/z calculated: 1077.37 $[M+2H]^{2+}$, 718.58 $[M+3H]^{3+}$; Observed m/z: 1077.42 $[M+2H]^{2+}$, 718.85 $[M+3H]^{3+}$

References

1. É. Bartus, Z. Hegedüs, E. Wéber, B. Csipak, G. Szakonyi,T.A. Martinek, De Novo Modular Development of a Foldameric Protein–Protein Interaction Inhibitor for Separate Hot Spots: A Dynamic Covalent Assembly Approach. *ChemistryOpen*. *6*(2), 236-241 (2017).

2. S.-Y. Lau, E. Procko,R. Gaudet, Distinct properties of Ca2+–calmodulin binding to N- and C-terminal regulatory regions of the TRPV1 channel. *Journal of General Physiology*. *140*(5), 541-555 (2012).